OPEN ACCESS

Impact of Cell Size and Format on External Short Circuit Behavior of Lithium-Ion Cells at Varying Cooling Conditions: Modeling and Simulation

Impact of Cell Size and Format on External Short Circuit Behavior of Lithium-Ion Cells at Varying Cooling Conditions: Modeling and Simulation

Alexander Rheinfeld, [z] Johannes Sturm, Alexander Frank, Stephan Kosch, Simon V. Erhard, and Andreas Jossen

Institute for Electrical Energy Storage Technology, Technical University of Munich (TUM), D-80333 Munich, Germany

A multidimensional multiphysics model is presented to describe the external short circuit behavior of lithium-ion cells of various formats and sizes at different convective cooling conditions. For this purpose, a previously published homogenized physical-chemical model of the external short circuit behavior of a small-sized lithium-ion cell was combined with an electrical and a thermal model to describe in-plane inhomogeneities in current density and heat generation rate throughout the electrodes, together with the resulting temperature distribution within the cell's jelly roll or electrode stack. With the investigated cylindrical, prismatic, and pouch-type cell formats combined with cell capacities ranging from consumer-sized to automotive applications, a comprehensive cell design study is presented during external short circuits. The investigated surface and tab cooling strategies reveal a limited cooling capability of each cell format and size, which seems to be defined by the ratio of cooled surface area to electrode area as well as the thermal resistivity of the respective cell geometry. The simulation results show that only thin cells with a large ratio of cooling surface to electrode area can be physically maintained within an uncritical operating window of cell temperature and state of charge in case a low-resistance external short circuit is applied.

Based on the comparably appealing combination of high energy and high power, lithium-ion batteries are the energy storage solution of choice for a manifold of today's applications, ranging from portable electronics to electric vehicles (EVs) and stationary energy storage systems. The increased electrochemical energy content required in order to achieve, for example, a longer battery run-time of portable electronics or an extended driving range of EVs, also comes with an increase in the thermal energy content which poses a significant hazard to customers and personnel involved in accidents. This tradeoff between energy increase and safety remains one of the main challenges of Li-ion battery research and development in order to achieve a high customer acceptance and, hence, market penetration. Besides the ever increasing demand for higher energy contents, key aspects of Li-ion battery safety are not fully understood so far, which hinders the efficient design of batteries that fulfill these two seemingly conflicting goals. Whilst Li-ion battery safety can be guaranteed on different levels of battery integration, the limited thermal stability of a cell's active and passive components can be often identified as the root cause for hazards that eventually need to be addressed on the cell, module, and battery pack or system level.

The vertical integration of battery safety, requires consideration of the topic throughout all relevant levels. This implies that a battery system needs to be designed in accordance with requirements defined by the applied materials and *vice versa*. The extremely complex interplay of safety relevant phenomena occurring on different length scales involving multiple mechanisms can often not be adequately described, which is why an experimental investigation of battery safety lacks true alternatives so far.

However, in order to efficiently design safe batteries, valid simulation tools are required to complement or even substitute costly and time-consuming safety and abuse tests. For commercial and larger sized Li-ion cells, such effort generally requires multidimensional modeling approaches describing multiphysics effects on varying length scales. Various approaches have been suggested throughout the past that can be generally divided into fully coupled continuum models[1] and models which decouple the prevailing length scale and geometry associated with a certain mechanism in order to reduce the computational effort,[2,3] such as the multidimensional modeling (MuDiMod) approach previously suggested by our group.[4–8] Mul-

tidimensional multiphysics models accounting for electrochemical, electrical, and thermal effects and interactions can be found rather frequently for what can be considered as "normal" operation of Li-ion cells. These models aim to describe local characteristics arising from in-plane polarization effects along the electrodes and a superimposed temperature distribution across the jelly roll or electrode stack. Such considerations then allow for deriving design criteria of cell properties linked to the electrochemical, electrical, and thermal behavior of the cell in order to guarantee a most optimized operation for a given application. Highly localized effects occurring during abnormal operation or abuse, such as those resulting from local short circuits triggered by an external deformation or penetration, can be adequately described by such an approach provided that no further reactions (e.g. exothermic side reactions) or effects (e.g. cell venting) are dominating the cell's behavior.[9–13]

Within this work, we extend the previously described MuDiMod approach[4–8] by accounting not only for a mapping between a spirally wound jelly roll and the cylindrical geometry it forms,[8] but by also describing prismatic and pouch-type cell geometries with either wound or stacked/folded electrode configurations. Furthermore, we include a validated physical-chemical short circuit model[14,15] describing the electrochemical behavior of the unit cell in order to depict the external short circuit behavior of cylindrical, prismatic, and pouch-type Li-ion cells of three different sizes, which are supposed to represent both consumer and automotive applications as can be found in hybrid electric vehicles (HEVs) and plug-in hybrid electric vehicles (PHEVs). Finally, a design study is carried out in order to evaluate the cooling capability of Li-ion cells depending on the cell's format and size as well as the applied cooling strategy, such as surface cooling and tab cooling, in terms of preventing a potential cell thermal runaway triggered by a low-resistance external short circuit.

Modeling and Simulation

Within this section, recent activities in multidimensional multiphysics modeling and simulation of Li-ion cells of different formats and sizes are briefly summarized. These works describe the context of the modeling approach presented here. For the reader's convenience, all relevant model parameters and equations are described in the appendix whereas the applied approach of multidimensional multiphysics coupling on varying length scales can be found in the

[z]E-mail: alexander.rheinfeld@tum.de

Table I. Overview of multidimensional multiphysics modeling approaches of Li-ion cells.

Cell format	Reference	Electrode configuration	Cell chemistry	Cell capacity	Electrode size/cm w_{ele}	h_{ele}	Model
Cylindrical	30	jelly roll	G/LMO	< 5 Ah	≈ 100	n.a.	2D-continuum
	31	jelly roll	G/NCA	19.9 Ah	323	13	3D-continuum
	41	jelly roll	G/LFP	> 5 Ah	≈ 111	11	720×p2D-EC/2D-E/3D-T
	8	jelly roll	SiC/NMC-811	3.35 Ah	61.5	5.8	197×p2D-EC/2D-E/3D-T
	4	jelly roll	G/LFP	2.5 Ah	169	5.6	19×p2D-EC/2D-E/2D-T
	60	jelly roll	G/LMO	≈ 2.9 Ah	158.2	6	18×p2D-EC/2D-E/1D-T
				≈ 24 Ah	620	14	
	38	jelly roll	G/LFP	2.3 Ah	169	5.6	1×p2D-EC/3D-T
	20	jelly roll	G/LMO	n.a.	19.1	5	56×p2D-EC/3D-E/3D-T
	27	jelly roll	G/LMO	0.5 Ah	≈ 100	n.a.	SPM-EC/2D-E/3D-T
Prismatic	32	jelly roll	G/NMC	40 Ah	512	20.5	3D-continuum (isothermal)
	41	jelly roll	G/LFP	> 5 Ah	≈ 111	11	672×p2D-EC/2D-E/3D-T
	61	jelly roll	G/NMC-111	25 Ah	n.a.	12.3	p2D-EC/3D-E/3D-T
	62	stack	G/LFP	16.5 Ah	6.7	10.5	p2D-EC/3D-E/3D-T
	63	stack	G/NCA	5 Ah	8	11	p2D-EC/3D-E/3D-T
	28	stack	G/NMC	5 Ah	12	7.5	42×SPM-EC/2D-E/2D-T
Pouch	1	stack	G/NCA	20 Ah	14	20	3D-continuum
	33	stack	G/LFP	10 Ah	10	11.5	3D-continuum
	7	stack	G/NMC-111	40 Ah	18	22	25×p2D/2D-E/2D-T
	6	stack	G/LCO	2.3 Ah	10	30	21×p2D/2D-E/2D-T/2D-M
	5	stack	G/NMC-111	0.8 Ah	49.8	9.8	11×p2D/ 2D-E
	20	stack	G/LMO	n.a.	50	2.4	1×p2D/3D-T
	39	stack	G/LFP	10 Ah	10	11.5	1×p2D-EC/3D-T
	40	stack	G/NMC-111	18.5 Ah	14.2	7.3	1×p2D-EC/3D-T
	3	stack	G/NCA	20 Ah	14.5	19.2	p2D-EC/2D-E/2D-T
	2	stack	G/LFP	n.a.	20	30	p2D/2D-E

p2D	homogenized pseudo two-dimensional Newman-type model
SPM	(enhanced) single particle model
EC	physical-chemical or empirical model describing the electrochemical unit cell
E	electrical model describing the current collectors
T	thermal model describing the jelly roll or electrode stack
M	mechanical model describing the jelly roll or electrode stack
2D/3D	two-/three-dimensional model geometry
G	Li_xC
SiC	3.5 wt% of Si in Li_xC
LCO	Li_yCoO_2
LFP	Li_yFePO_4
LMO	$Li_yMn_2O_4$
NCA	$Li_yNi_{0.8}Co_{0.15}Al_{0.05}O_2$
NMC-111	$Li_yNi_{1/3}Co_{1/3}Mn_{1/3}O_2$
NMC-811	$Li_yNi_{0.8}Co_{0.1}Mn_{0.1}O_2$

supplementary material for all three cell formats studied within this work.

Modeling the electrochemical-thermal behavior of the electrochemical unit cell together with polarization effects across and along the electrodes, as well as the thermal behavior of cell's jelly roll or electrode stack, the size of the differential algebraic equation (DAE) system is considerably increased. The associated computational effort to solve the DAE system, however, needs to be limited in order to not only guarantee an efficient simulation of the cell's behavior but to allow for a successful or converging calculation in the first place.

Based on the extremely large currents occurring during short circuits involving considerable gradients in potential and concentration across the electrode thickness,[16,17] discretizing and, hence, calculating the electrochemical response of the unit cell requires comparably large computational effort. Neglecting a spatial discretization between the electrodes by applying, for example, linear polarization models, such as suggested by Newman and Tiedeman[18] as well as its modifications,[19–22] seems not to be an appropriate choice as previously described rate limiting mechanisms defining a cell's short circuit

behavior cannot be considered.[15] An adequately limited applicability during short circuit scenarios holds for equivalent circuit models (ECMs)[23–25] as well as single particle models (SPMs) and associated extensions.[26–29]

Recent works that are relevant for the considerations presented here are summarized in Table I. As can be seen from the table, there is a rather even split between works focusing on spirally wound electrode configurations (jelly roll), as found in cylindrical or prismatic cells, and stacked electrode configurations, as found in prismatic and pouch-type cells. With a wide variety of cell chemistries, capacities, and sizes, a manifold of multiphysics coupling schemes have also been applied, ranging from continuum models to geometrically decoupled models. Most of the presented models focus on simultaneously depicting the electrochemical processes occurring between anode and cathode based on solid and liquid phase concentrations and potentials, the electrical characteristics along the planar electrodes, and the thermal behavior across the cell's electrode configuration. Multidimensional continuum models[1,30–33] often lack computational efficiency as all considered variables ideally need to be solved within the same discretiza-

tion scheme, which is dominated by the smallest geometric entity (i.e. anode, separator, cathode, and current collector domains). Whilst such fine discretization is vital for describing the electrochemical response of the cell especially at higher currents, a coarser discretization would still allow for sufficient modeling accuracy in terms of the electrical and thermal cell behavior. This partly explains why this model type is not applied to the same extent as geometrically decoupled modeling approaches (see Table I). Such geometrical decoupling often involves studying electrochemical, electrical, thermal, and even mechanical effects on the corresponding lengths scales and exchanging only relevant variables between the individual models such as temperature, potential, current density distribution, and heat generation rate.

By describing mass and charge transport throughout the thickness of the electrodes and separator as well as diffusion limited reaction kinetics and diffusion processes within the active material particles (1D+1D, i.e. p2D[34,35]), the electrochemical cell behavior can be reliably described over a wide range of currents and temperatures.[15,16] By further accounting for a potential distribution and current flux along the current collectors (2D[2,18]), inhomogeneities in current density distribution and, hence, heat generation rate can be described. By finally accounting for sensible heat effects, heat conduction, and heat exchange of the cell with its surroundings, the resulting cell temperature and temperature distribution along the electrodes can be calculated based on a 2D[4,6,7] or 3D[8] thermal representation of the cell. Such considerations are essential as even under "normal" operation not only considerable variations in current density distribution and, consequently, state of charge (SoC) can be observed along the electrodes,[5] but also severe temperature gradients need to be considered which influence the local electrochemical and electrical cell behavior.[21,36,37] Whilst most of the presented geometrically decoupled multidimensional multiphysics models rely on a not further specified 2D electrical model of the current collector foils and a 1D to 3D thermal model of the cell's geometry or electrode configuration depending on the cooling condition and applicability of symmetry planes, the geometrical arrangement of the electrochemical models, such as p2D and SPM, greatly varies from coupling only one model node[38–40] to several hundred model nodes[8,41] to the planar electrical electrode model.

Within this work, very large currents and heat generation rates as well as cooling rates are applied to cells of various formats and sizes. This requires not only a high discretization of the used p2D

physical-chemical modeling approach in order to describe the electrochemical unit cell,[15] but also demands for a precise, numerically efficient bi-directional mapping between the thermal and electrical/electrochemical response of the cell. Only few works have previously reported using a local coordinate mapping between a 2D electrical and 3D thermal model of a cylindrical cell.[24,27] Such mapping has been recently adapted for the MuDiMod approach[8] which is extended in this work to also describe the mapping between a spirally wound electrode configuration for a prismatic cell as well as a z-folded electrode configuration for a pouch-type cell (see supplementary material). Combining this coupling scheme with the previously published validated p2D short circuit model,[14,15] the desired cell design study can be carried out in order to evaluate the cooling capability of cells of different format and size during low-resistance external short circuits.

The validated physical-chemical model represents a Li-ion cell formed of graphite as anode and $LiNi_{1/3}Co_{1/3}Mn_{1/3}O_2$ (NCM-111, in the following written as NMC-111) as cathode active materials containing 1 M $LiPF_6$ in ethylene carbonate (EC) : dimethyl carbonate (DMC) 1:1 (by weight) with 2 wt% vinylene carbonate (VC) as electrolyte. An effective electrode loading of 1.85 mAh cm^{-2} (i.e. a balanced electrode loading, BA[14]) between an upper and lower cell voltage of 4.2 V and 3.0 V is considered, as represented by the material and electrode parameters summarized in the appendix. The geometric characteristics of the studied cylindrical, prismatic, and pouch-type cells with capacities of 3 Ah (consumer-sized), 9 Ah (HEV-sized), and 27 Ah (PHEV-sized) within this voltage range are shown in Table II. The aspect ratio of each individual cell format was kept constant for all considered cell sizes. Whilst a 26650 consumer-sized cell was used as the targeted geometry for the cylindrical cells, a PHEV2-format was considered for the prismatic cells, and a combination of a PHEV1-format and BEV1-format was applied for the pouch-type cells.[42] The PHEV/BEV cell geometry for the prismatic and pouch-type cells was taken from DIN 91252.[42] All cell formats are considered to contain electrodes and a counter-tab configuration with a continuous electrical interconnection along the electrode width w_{ele}. Whilst such electrode configuration can be more usually found within larger-sized cylindrical and prismatic Li-ion cells, a stacked or z-folded electrode configuration realistically requires individual electrode sheets with similarly individual or z-folded separator configurations. However, for model simplicity, a continuous electrode configuration is also considered for

Table II. Geometric characteristics of studied cell formats and sizes.

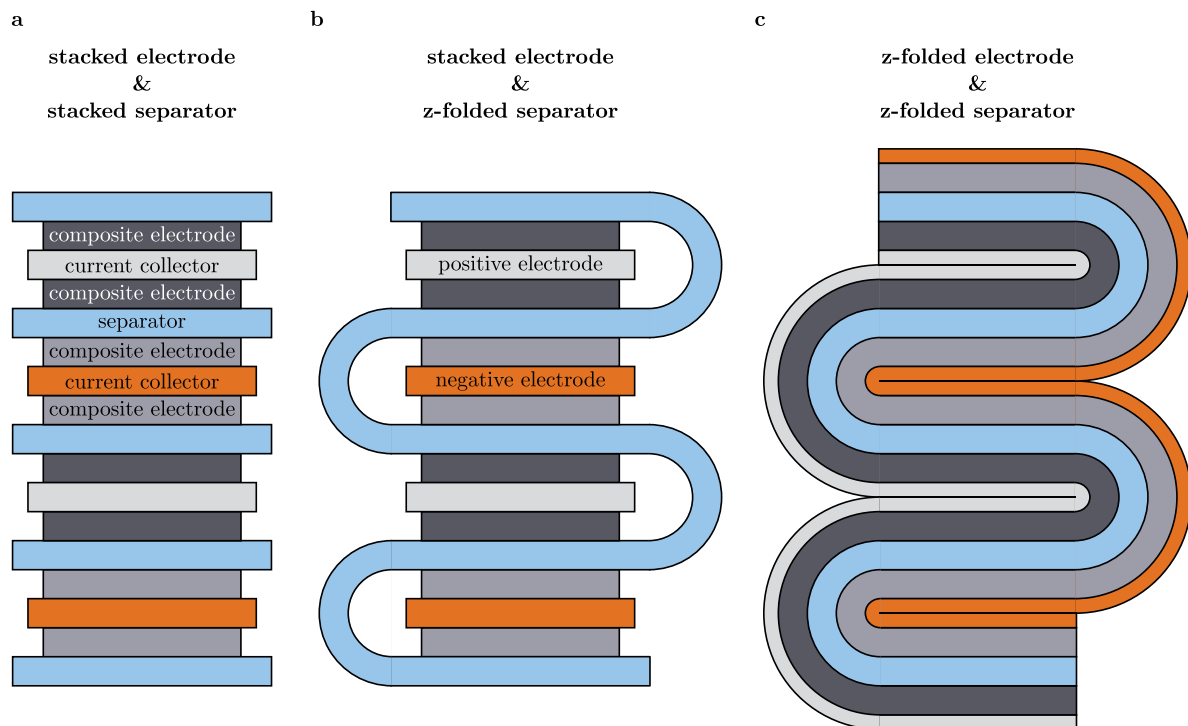| Cell size	Cell capacity	p2D-discretization $w_{ele} \times h_{ele}$	Description	Unit	Cylindrical	Prismatic	Pouch
Consumer	3 Ah	4×3	w_{ele}	mm	1361.9	1170.7	744.8
			h_{ele}	mm	59.5	69.2	108.8
			w_{jelly}, w_{stack}	mm		41.3	47.7
			h_{jelly}, h_{stack}	mm	59.5	69.2	108.8
			d_{jelly}, d_{stack}	mm	25.4	12.4	5.6
			A_{surf}/A_{ele}	%	2.9	4.1	6.4
			A_{tab}/A_{ele}	%	0.6	0.5	0.3
HEV	9 Ah	9×4	w_{ele}	mm	2834.5	2460.5	1549.2
			h_{ele}	mm	85.8	98.8	156.9
			w_{jelly}, w_{stack}	mm		59.0	68.7
			h_{jelly}, h_{stack}	mm	85.8	98.8	156.9
			d_{jelly}, d_{stack}	mm	36.7	17.7	8.4
			A_{surf}/A_{ele}	%	2.0	2.8	4.4
			A_{tab}/A_{ele}	%	0.4	0.4	0.2
PHEV	27 Ah	18×6	w_{ele}	mm	5898.8	5153.9	3222.4
			h_{ele}	mm	123.6	141.5	226.3
			w_{jelly}, w_{stack}	mm		84.5	99.2
			h_{jelly}, h_{stack}	mm	123.6	141.5	226.3
			d_{jelly}, d_{stack}	mm	52.9	25.4	12.1
			A_{surf}/A_{ele}	%	1.4	1.9	3.1
			A_{tab}/A_{ele}	%	0.3	0.3	0.2

Figure 1. Modeled z-folded electrode and separator configuration forming the electrode stack of the pouch-type cell considered in this work (c) in comparison to common electrode and separator configurations including stacked, double-coated electrode sheets as well as individual separators (a) or a continuous, z-folded separator (b) in between the positive and negative electrodes.

the pouch-type cell assuming a z-folded electrode and separator configuration, as the polarization along the height of the electrode (i.e. between the tabs) is assumed to dominate the in-plane electrical behavior of the electrodes which is, hence, considered to be only marginally affected by the electrical electrode configuration along the width of the electrode. This essentially implies that the usually double-sided electrodes are considered to be coated only on one side with half the current collector thickness. This approach is schematically shown in Fig. 1c in comparison to a strictly stacked electrode and separator configuration (see Fig. 1a), as well as an electrode stack including a z-folded separator (see Fig. 1b).

For the applied cooling strategies, either the surface area of the cell or the tab area was used applying a convective boundary condition with convection coefficients h_c (W m^{-2} K^{-1}) ranging from natural convection (1 W m^{-2} K^{-1}) to an immediate phase change (10^5 W m^{-2} K^{-1}) at a constant coolant temperature of 25°C. This range is chosen in order to evaluate the cell's cooling behavior under physical extremes and does not necessarily reflect a realistic scenario (e.g. water would need to be held far below ambient pressure to realize such high heat transfer coefficients including boiling at 25°C). Furthermore, the applied convective cooling is considered to directly affect the surface of the cell's jelly roll or electrode stack which is not the case in real life as an additional cell housing would need to be considered. This assumption forms a best case which neglects the comparably low thermal resistivity of the cell's housing as well as geometrical imperfections of both cell and cooling system (e.g. unevenness resulting in a reduced thermal contact area). Radiation effects are further neglected as the cell is expected to be directly in contact with a cooler or the coolant. For the pouch-type cell, only the large surface area planar to the electrodes is considered for surface cooling whilst the entire lateral surface area of the jelly roll is considered for the prismatic and cylindrical cell under this cooling condition. Moreover, exothermic side reactions occurring at elevated temperatures as previously described[43–46] are not considered in this work in order to reduce computational time.

With the PHEV-sized cells requiring the largest discretization effort, the chosen 108 p2D models per electrode pair (or 8 p2D models

per Ah) mark the upper limit of degrees of freedom that the solver and workstation are able to handle efficiently for the required discretization of the p2D model during high rate operation (COMSOL Multiphysics 5.3a, Intel Xeon E5-2687W 0 3.1 GHz with 64 GB RAM). A higher in-plane discretization was not feasible due to the large through-plane discretization effort required by the p2D models at very high currents. In our previous work, 158 p2D nodes per electrode pair were considered as the maximum for a lower discretization of the p2D models using the same computational resources.[8] In order to allow for maximum comparability, the same discretization of 8 p2D nodes per Ah was chosen for all cell models. Depending on numerical convergence, solving the PHEV-models required approximately two to three days per cell and cooling condition, whereas the consumer-sized models were generally solved within less than six hours.

Results and Discussion

Within this section, first of all the electrochemical-thermal short circuit behavior of a graphite/ NMC-111 electrochemical unit cell is studied. This is achieved by neglecting any electrical and thermal effects associated with geometric constraints of planar electrodes, which are usually spirally wound or stacked to form larger-sized Li-ion cells, as found in commercial applications. Assuming an ideal thermal contact of the electrodes to the cell's surroundings, the impact of various cooling conditions is studied by means of the p2D modeling approach described in the previous section and the appendix. By further accounting for geometrical characteristics of cylindrical, prismatic, and pouch-type Li-ion cells (see Table II), the external short circuit behavior of larger-sized Li-ion cells is studied by the MuDiMod approach described in the previous section, the appendix, and the supplementary material. The impact of a cell's size and format or configuration of the stacked or wound electrode is studied under various cooling conditions which are related to the simulation studies carried out with the p2D model of the electrochemical unit cell. These two approaches allow an examination of the impact of a cell's geometry on its cooling capabilities. The presented simulation results are further used as an
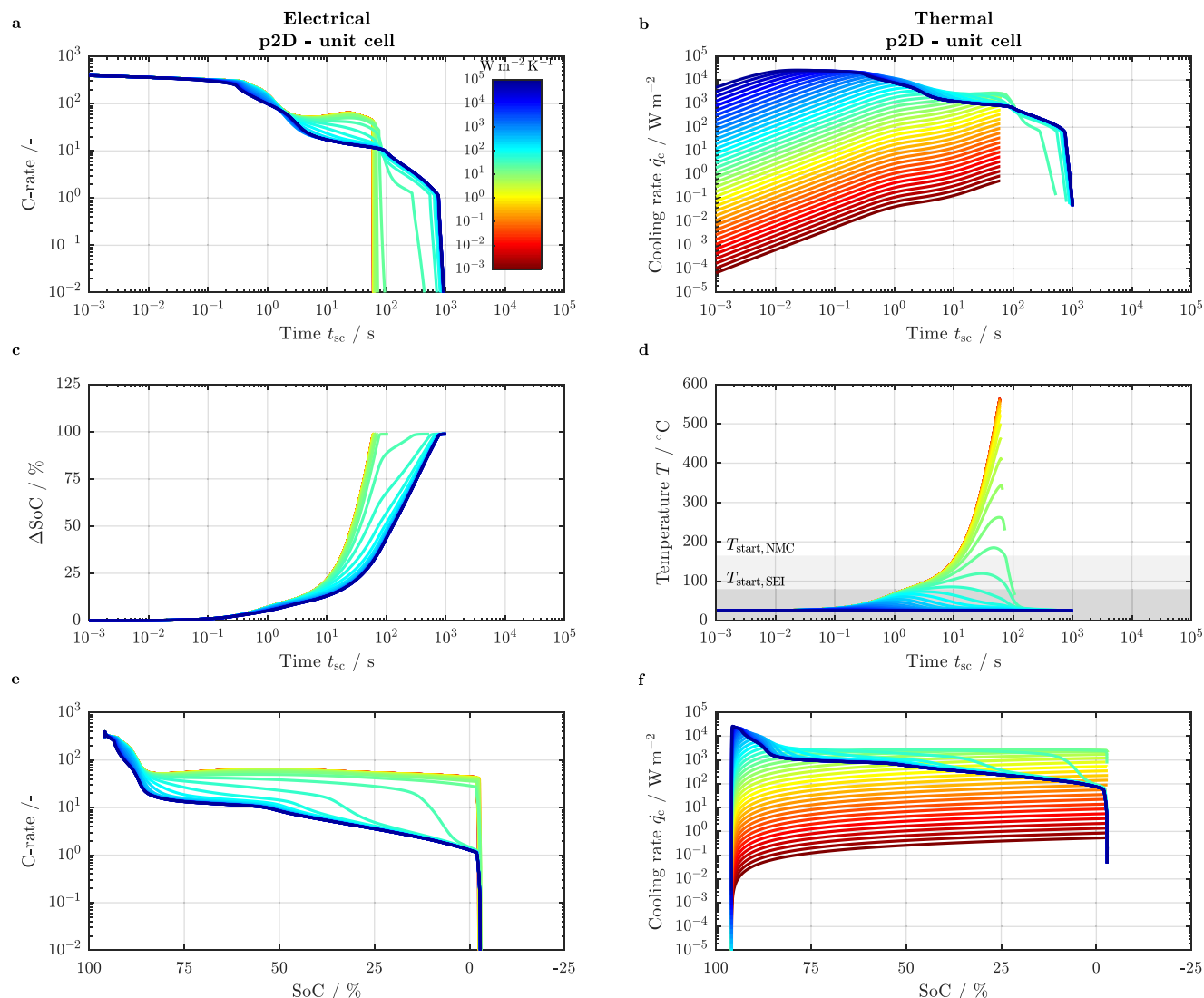
Figure 2. Predicted electrochemical (left: a, c, and e) and thermal response (right: b, d, and f) of the studied electrochemical unit cell under various cooling conditions with convection coefficients h_c ranging from 10^{-3} W m^{-2} K^{-1} to 10^5 W m^{-2} K^{-1} and a constant coolant temperature of 25°C as a function of short circuit duration t_{sc} (a to d) and as a function of SoC (e and f) for the C-rate (a and e), cooling rate $\dot{q}_c$ (b and f), ΔSoC (c), and temperature T (d). The coloring represents the chosen range of convection coefficients as defined in a.

indication of the feasibility of cooling cells of various sizes and formats during short circuit conditions, which may allow a reduction in the likelihood of cell thermal runaway.

Electrochemical-thermal short circuit behavior of the electrochemical unit cell.—By applying a "hard" external short circuit condition with a low resistance to the studied electrochemical unit cell within the p2D model as previously reported (i.e. applying a boundary condition approaching a cell voltage of 0 V),[15] the transient short circuit behavior of the cell can be studied in great detail. With electrode area specific convection coefficients h_c ranging from almost adiabatic conditions (10^{-3} W m^{-2} K^{-1}) to cooling conditions approaching isothermal operation involving immediate phase change, such as boiling or evaporation of the coolant (10^5 W m^{-2} K^{-1}), the dependency of the cell's short circuit behavior on the prevailing thermal boundary conditions can be evaluated, as shown in Fig. 2. As can be seen from the figure, a considerably strong convective cooling results in a short circuit behavior of the studied cells as recently reported under quasi-isothermal test conditions.[14,15] With lower heat transfer coefficients and, hence, lower cooling, the reported step-like characteristics

in C-rate as a function of short circuit duration t_{sc} (s) and SoC changes toward higher C-rates, forming a peak-like shape around 30 s which correlates to approximately 50% SoC (see Figs. 2a and 2e). This increase in C-rate, which can be generally explained by enhanced transport properties of the liquid electrolyte[47] and increased solid phase diffusion coefficients of the active materials at elevated temperatures,[17] generally results in an accelerated short circuit behavior with a faster discharge as previously discussed (see Figs. 2a and 2c).[14,15] Based on this fast discharge converting the electrochemically stored energy into thermal energy, the temperature of the studied unit cell also quickly rises beyond the starting temperatures of exothermic side reactions involving the cell's components. The exothermic decomposition reaction of the graphite anode's solid electrolyte interphase (SEI) starts around 80°C with comparably low heat generation,[44,48,49] whereas, in the presence of non-aqueous electrolytes, cathode materials such as NMC start to exothermically decompose from as high as 180°C for NMC-111 to as low as 120°C for LiNi$_{0.8}$Co$_{0.1}$Mn$_{0.1}$O$_2$ (NMC-811) depending on the composition of NMC.[50] This decomposition reaction involving oxygen release is accompanied by comparably large heat rates that may result in electrolyte oxidation and, eventually, cell
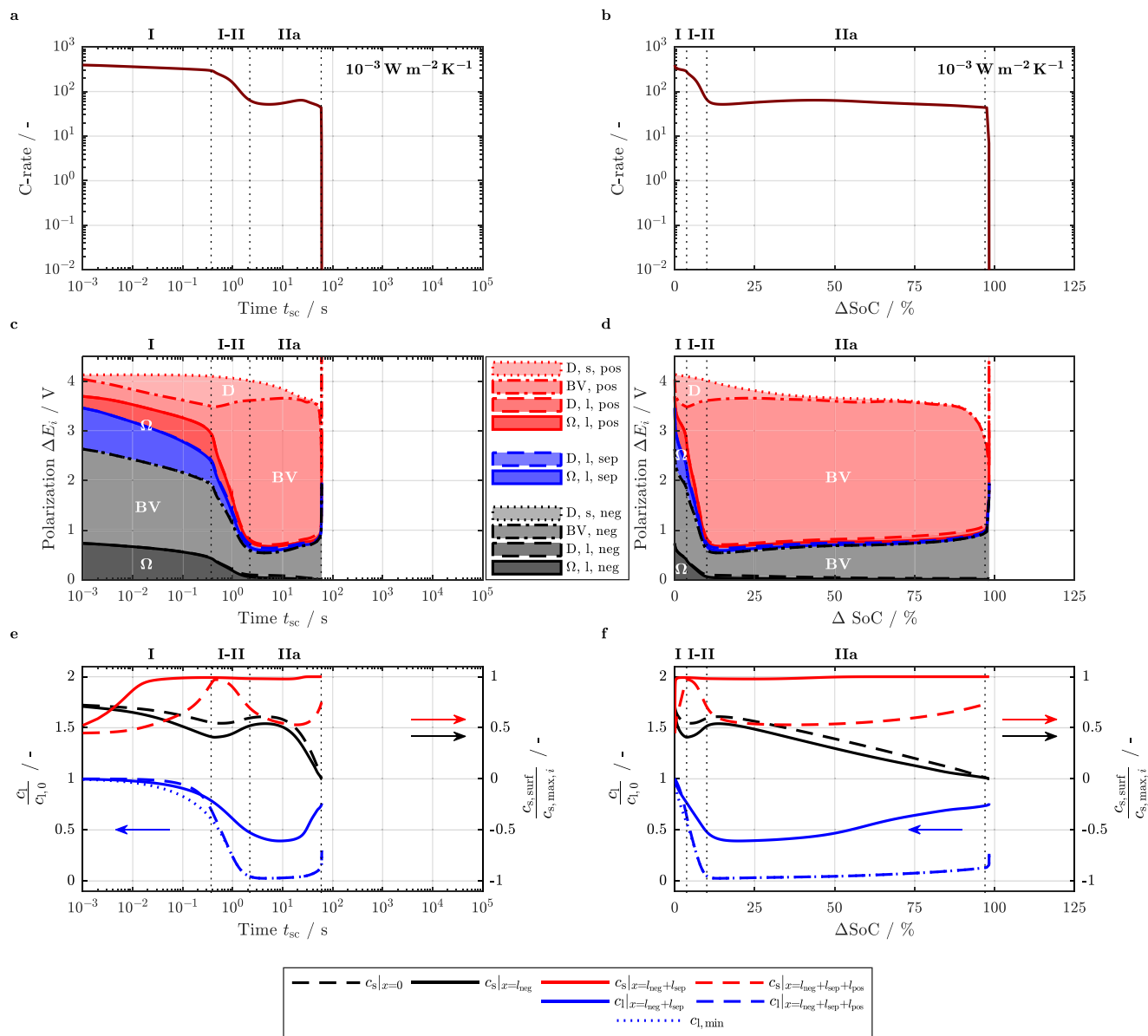
Figure 3. Predicted phases of a short circuit during a hard short circuit event for a cooling condition of 10^{-3} W m^{-2} K^{-1} with respect to electrode area and a coolant temperature of 25°C observed in C-rate (top: a and b), the corresponding polarization throughout the electrodes and separator (middle: c and d) resulting from the normalized solid (surface) and liquid phase concentration (average) at distinct locations of the cell (bottom: e and f) as a function of short circuit duration (left: a, c, and e) and as a function of normalized discharged capacity (right: b, d, and f). The overall polarization (middle: c and d) is primarily based on the contribution of diffusion related losses (D) and ohmic losses (Ω) within the solid (s) and liquid (l) components of the negative (neg) and positive electrode (pos) as well as throughout the separator (sep) including overpotentials associated with Butler-Volmer reaction kinetics (BV). Ohmic losses within the solid phase are negligible in comparison.

thermal runaway. Within this work, a starting temperature of approximately 165°C of the exothermic side reactions involving NMC is considered as previously reported for LiNi$_{0.4}$Co$_{0.2}$Mn$_{0.4}$O$_2$ (NMC-442) at 100% SoC.[46] This exemplary temperature threshold is chosen in order to not represent an overly optimistic scenario with rather high starting temperatures but to approach a more realistic application with moderate nickel contents within the NMC composition such as NMC-442, NMC-532, and NMC-622 or, in other words, to evaluate an NMC composition which is not limited to NMC-111 alone. The chosen starting temperature of 165°C was derived by Hildebrand et al. by means of a model-based data analysis from two-component calorimetric measurements formed of NMC-442 and electrolyte.[46]

With increasing convection coefficient and cell temperature, the electrode area specific cooling rate $\dot{q}_c$ (W m^{-2}) increases according to Newton's law of cooling (see Figs. 2b and 2f). Interestingly, there seems to be a threshold convection coefficient at which the cooling rate dominates the cell's short circuit behavior, resulting in a significantly decelerated discharge with lower C-rates and heat generation rates accompanied by a reduced cooling demand with ongoing short circuit duration. This correlates to a fading of the observed peak in C-rate resulting in the previously reported step-like behavior under quasi-isothermal conditions accompanied by a varying inclination in C-rate throughout the second plateau at approximately 80 s or 55% SoC (see blue line in Figs. 2a and 2e).[14,15] The discussed change in inclination of the C-rate, both as a function of short circuit

duration t_{sc} and SoC, can be correlated to a transient change in rate limiting mechanisms within the NMC cathode. In the beginning of the second plateau, rate limitation is based on a depletion of Li-ions within the liquid electrolyte near the current collector and a simultaneous saturation of the surface concentration of the active material particles near the separator. With ongoing short circuit duration, the short circuit behavior is exclusively dominated by solid phase diffusion limitations within the NMC cathode, resulting in a varying slope of the C-rate curve (see blue line Figs. 2a and 2e).[15] By varying the electrode area specific heat transfer coefficient h_c, a different behavior can be observed for non-isothermal conditions as shown in Fig. 2 and Fig. 2. Compared to the previously reported breakdown in cell polarization for isothermal conditions at high cooling rates (see Fig. A1 in the appendix),[15] an increase in temperature throughout the short circuit duration results in a minor contribution of solid phase diffusion polarization after the first plateau (I) and the transition toward the second plateau (I-II), especially within the cathode (see Fig. 3).

As a consequence, the overall cell polarization throughout the second plateau (II) is primarily dominated by reaction kinetics within the positive electrode based on a depletion in salt concentration within the liquid electrolyte near the current collector and a simultaneous approach of a fully saturated surface concentration within the active material particles near the separator (IIa). As the simulated temperatures exceed the starting temperature of exothermic side reactions, a limitation of charge transfer kinetics originating in a fully saturated positive electrode at the surface of the active material particles cannot be observed (previously reported as stage IIb,[15] see Fig. A1 in the appendix). Despite the compromised validity of the model at elevated temperatures neglecting exothermic side reactions, the predicted increased current levels also come with a stronger contribution from charge transfer overpotentials within the negative electrode throughout the short circuit duration which can be correlated to losses associated with the resistivity of the SEI. Furthermore, the observed peak in C-rate around 30 s or 50% SoC forms as soon as a fully saturated surface concentration is reached at the separator interface of the positive electrode even though ion transport within both solid and liquid components is enhanced with increasing temperature. A similar peak-like behavior during external short circuits has been previously reported via modeling and simulation[16,17,51] as well as experiments.[52]

With the observation of a strongly decelerated short circuit behavior by increasing the electrode area specific convection coefficient h_c, a threshold convection coefficient can be identified at which exothermic side reactions can be avoided completely or at least delayed toward uncritical SoCs (see Fig. 2). With this in mind, either the maximum temperature occurring throughout the short circuit or the temperature at a defined SoC can be evaluated as shown in Fig. 4.

Within this work, exothermic side reactions triggered within the NMC cathode at an SoC of 50% or less are considered as uncritical resulting in no cell thermal runaway, as previously observed via accelerating rate calorimetry measurements of pouch-type Li-ion cells formed of mesocarbon microbeads (MCMB) and NMC-442.[46] This can be explained with a reduced overall reactivity of both anode and cathode with lower heat generation rates at lower SoCs.[46] At this SoC, the starting temperature of the decomposition reaction of NMC-442 has been reported to slightly increase toward 170°C. However, for simplicity reasons, a constant starting temperature of 165°C is considered in this work for the NMC cathode. Even though exothermic side reactions involving SEI decomposition are triggered at lower temperatures,[48,49] such reactions are not considered to be sufficient enough to result in cell thermal runaway in this work, due to the comparably low heat released throughout this process.[53] Both the maximum temperature T_{max} occurring throughout the short circuit duration and the temperature at 50% SoC $T|_{50\% SoC}$ are studied in Fig. 4. As can be seen from the figure, with an electrode area specific convection coefficient ranging from approximately 20 W m^{-2} K^{-1} to 55 W m^{-2} K^{-1}, not only exothermic side reactions within the positive electrode can be delayed toward uncritical SoCs (i.e. $T|_{50\% SoC} < T_{start, NMC}$) but
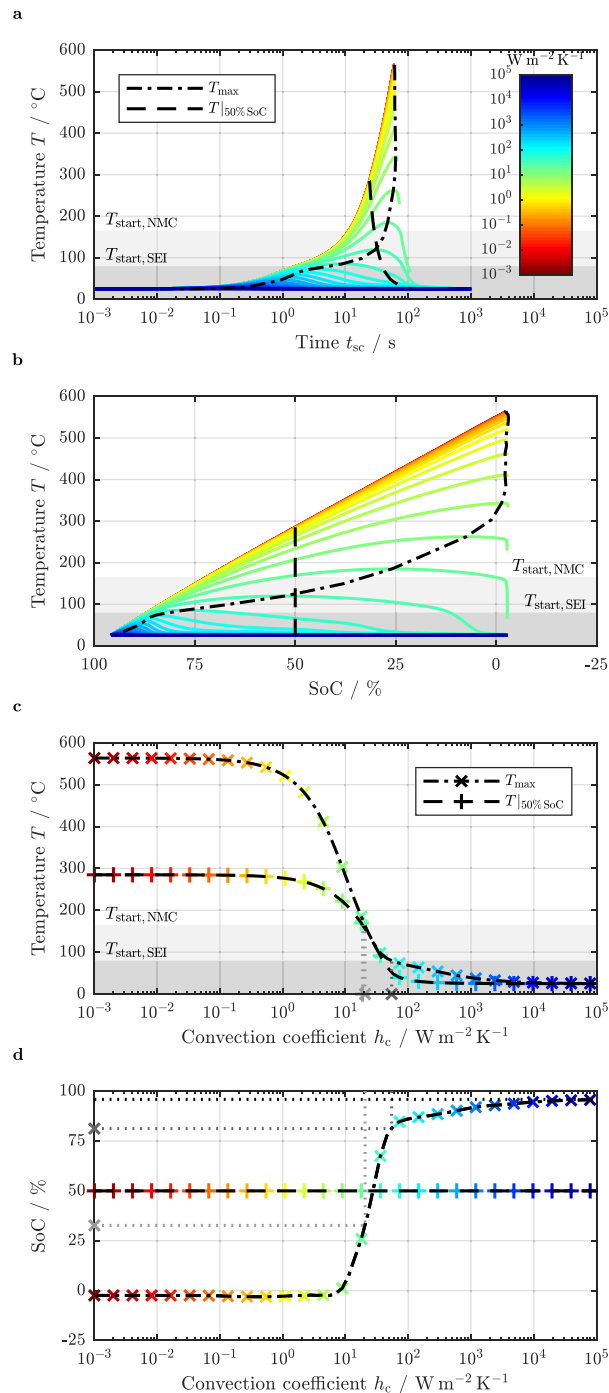

Figure 4. Predicted temperature of the electrochemical unit cell at a coolant temperature of 25°C as a function of short circuit duration t_{sc} (a), as a function of SoC (b), and as a function applied electrode area specific heat transfer coefficients h_c indicating the maximum occurring cell temperature T_{max} (dash-dotted line) and the cell temperature at 50% SoC $T|_{50\% SoC}$ (dashed line) for varying h_c (colors as defined in a) allowing for deriving cooling requirements to keep the unit cell within an uncritical temperature (c) and SoC window (d). Colored markers in c indicate the intersection of the dash-dotted (T_{max}: ×) and dashed lines ($T|_{50\% SoC}$: +) with the cell temperature curves shown in a and b as a function of h_c. The cell SoC corresponding to this intersection is shown in d. Gray markers in c and d indicate the minimum value of h_c and associated SoC to fall below a certain temperature threshold (i.e. $T_{start, SEI}$ or $T_{start, NMC}$) outlined as gray shaded areas in a, b, and c.
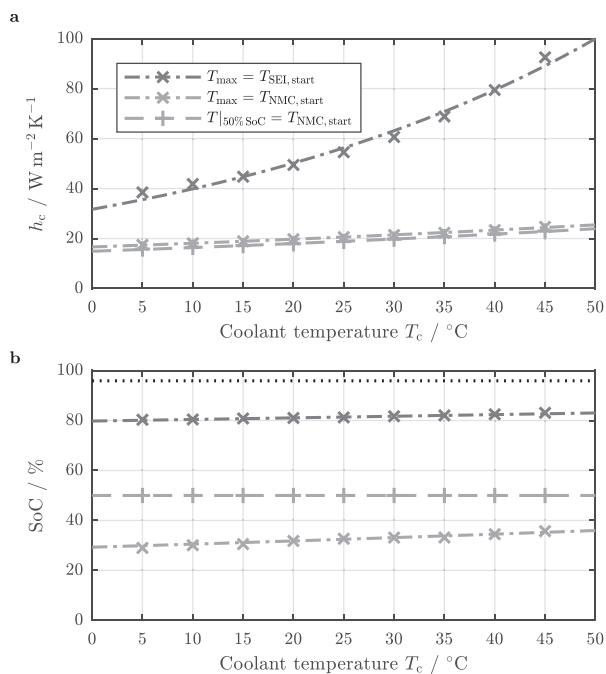
Figure 5. Comparison of electrode area specific convection coefficients h_c for predicted cooling requirements to avoid exothermic side reactions during hard short circuit events applied to the electrochemical unit cell as a function of coolant temperature ranging from 5°C to 45°C at an initial cell temperature of 25°C (a) and associated cell SoC (b) in accordance with Figs. 4c and 4d.

also exothermic side reactions within the anode can be ruled out completely (i.e. $T_{max} < T_{start, SEI}$, see Fig. 4c). Whilst electrode area specific convection coefficients h_c below 1 W m^{-2} K^{-1} merely reduce the resulting temperature of the unit cell due to the negligible cooling effect despite the large temperature difference between cell and coolant (see see Figs. 4a, 4b, and 4c), values above 100 W m^{-2} K^{-1} result in an asymptotic approach of the coolant temperature for both temperature criteria (see Fig. 4c). Between these two values, a strong variation in resulting cell temperature (see T_{max} and $T|_{50\% SoC}$ in Fig. 4c) and associated SoC (see T_{max} in Fig. 4d) can be observed, marking the range of interest for deriving appropriate cooling strategies. In order to allow for a complete avoidance of exothermic side reactions, the maximum temperature T_{max} needs to stay below the starting temperature of the SEI decomposition reaction $T_{start, SEI}$ of approximately 80°C. In order to achieve this, the short circuited cell needs to be cooled down below this temperature threshold within the first 15% ΔSoC or approximately 10 s of the short circuit. This leaves only little time between detecting a short circuit to applying an emergency cooling (see Figs. 2c and 2d and dash-dotted line as well as dark gray markers in Figs. 4c and 4d), starting from approximately 96% SoC in accordance with previous work.[15] In order to completely avoid exothermic side reactions involving the NMC cathode $T_{start, NMC}$ at approximately 165°C, the maximum temperature occurring throughout the short circuit must be maintained below this temperature within a ΔSoC of approximately 60%, which also implies a higher tolerance to a delay between short circuit detection and cell cooling (see dash-dotted line as well as light gray area and markers in Figs. 4c and 4d). The aforementioned criterion of approaching $T_{start, NMC}$ at 50% SoC can be therefore understood as a minimum cooling requirement to avoid cell thermal runaway whilst allowing for exothermic side reactions to occur within both anode and cathode. The range of the different cooling requirements are compared in Fig. 5a as a function of coolant temperature. As can be seen from
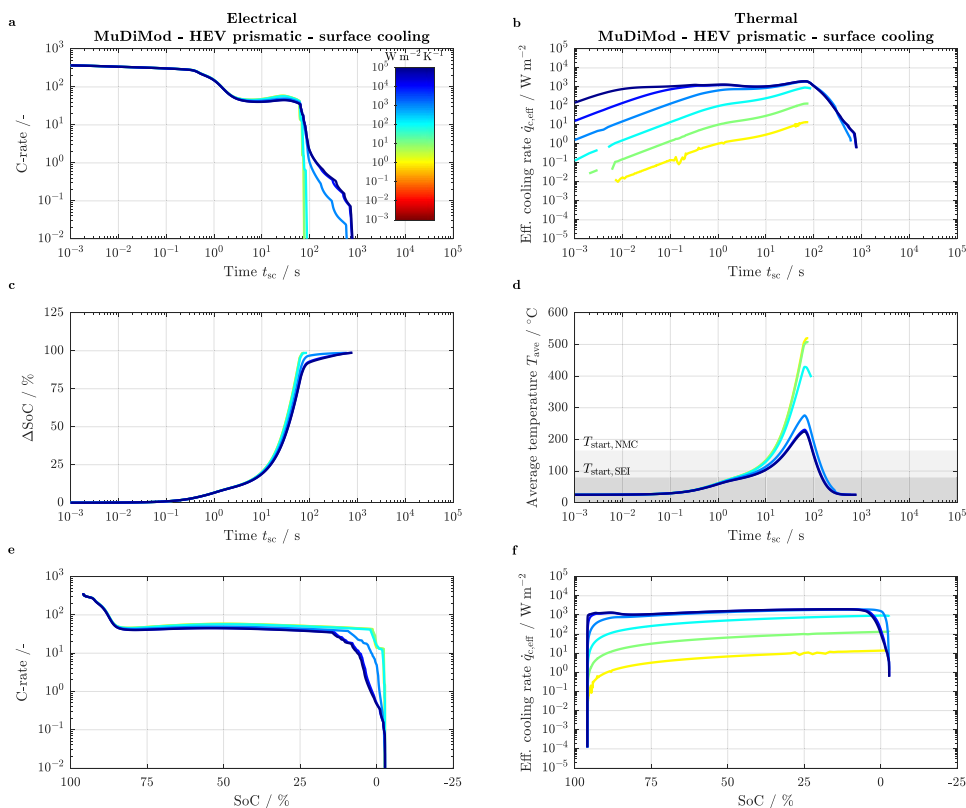

Figure 6. Predicted electrochemical (left: a, c, and e) and thermal response (right: b, d, and f) of the studied HEV-sized prismatic cell under various cooling conditions applying a surface cooling with convection coefficients h_c ranging from 1 W m^{-2} K^{-1} to 10^5 W m^{-2} K^{-1} and a constant coolant temperature of 25°C as a function of short circuit duration t_{sc} (a to d) and as a function of SoC (e and f) for the C-rate (a and e), the effectice cooling rate $\dot{q}_{c, eff}$ (b and f), ΔSoC (c), and average temperature T_{ave} (d).
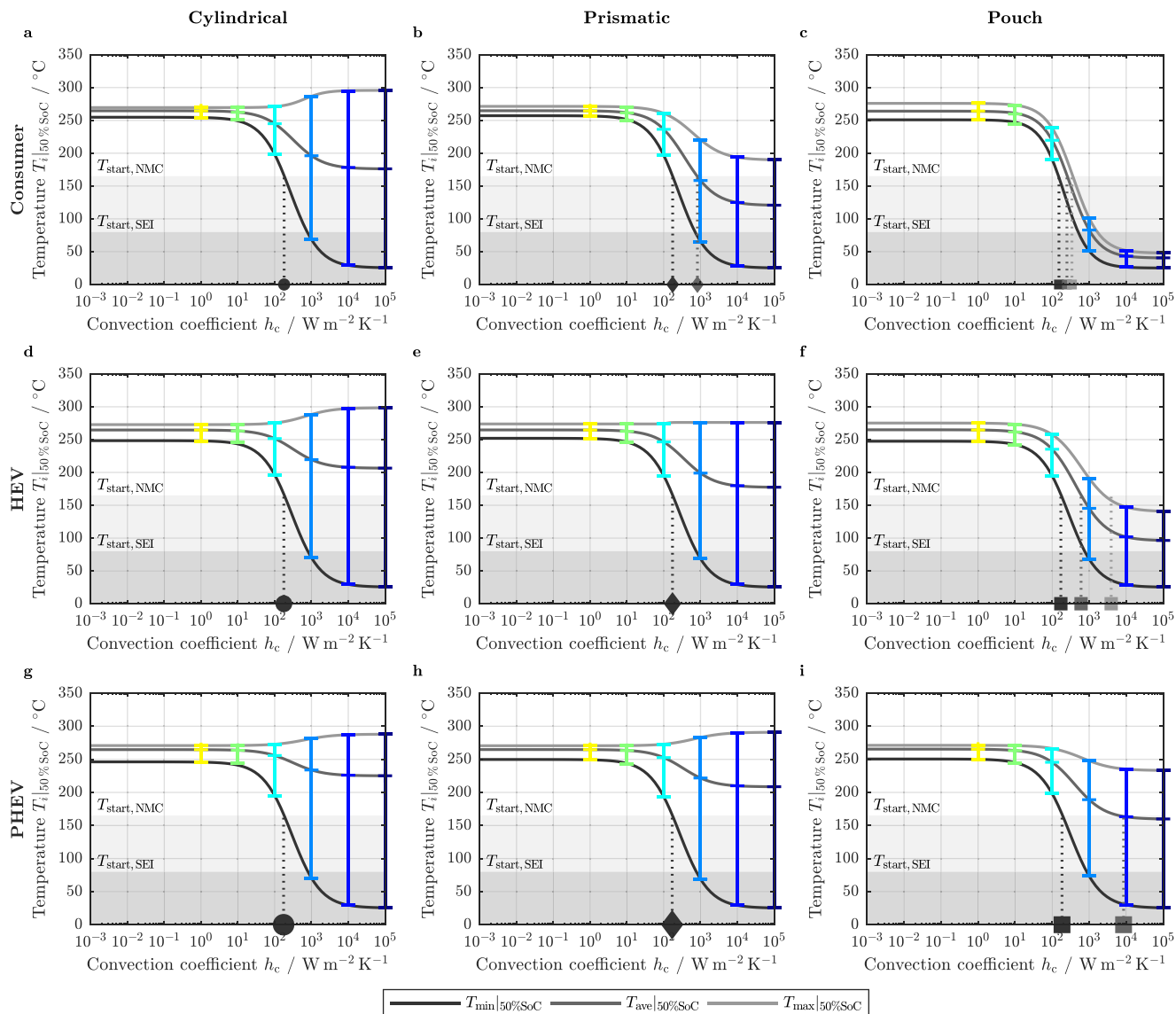
Figure 7. Predicted minimum, average, and maximum temperature of the studied cell formats and sizes in accordance with Table II for consumer-sized (top: a, b, and c), HEV-sized (middle horizontal: d, e, and f), and PHEV-sized (bottom: g, h, and i) cylindrical (left: a, d, and g), prismatic (middle vertical: b, e, and h), and pouch-type cells (right: c, f, and i) at an average cell SoC of 50% applying a surface cooling with convection coefficients h_c ranging from 1 W m^{-2} K^{-1} to 10^5 W m^{-2} K^{-1} and a constant coolant temperature of 25°C as a function of h_c. The vertical dotted lines and markers indicate a cooling below the threshold temperature $T_{start, NMC}$ for each individual temperatures. Colors are chosen in accordance with Figs. 2, 4, and 6.

the figure, h_c is considerably dependent on the coolant temperature for T_{max} approaching $T_{start, SEI}$. In order for both T_{max} and $T|_{50\% SoC}$ to fall below $T_{start, NMC}$, a reduced impact of the coolant temperature can be observed. This implies that for lower coolant temperatures, the likelihood of completely avoiding exothermic decomposition reactions can be considerably increased, approaching the minimum cooling requirements set by the $T|_{50\% SoC} = T_{NMC}$ criterion. However, this has almost no effect on the tolerable ΔSoC range, implying the necessity of a comparably immediate cooling of the cell in order to achieve this goal (see Fig. 5b). For both T_{max} and $T|_{50\% SoC}$ to approach $T_{start, NMC}$, similar values for h_c can be observed with a larger tolerable ΔSoC for T_{max} compared to $T|_{50\% SoC}$ at slightly higher values of h_c.

In this work, $T|_{50\% SoC} = T_{start, NMC}$ is considered as the minimum cooling requirement in order to be able to avoid cell thermal runaway which will be studied in further detail for varying cell formats and sizes whilst applying a coolant temperature of 25°C.

Electrochemical-electrical-thermal short circuit behavior of different cell formats and sizes.—By applying the MuDiMod approach in order to describe the cell formats and sizes shown in Table II, the external short circuit behavior of larger sized cells used for commercial applications can be evaluated in comparison to the discussed short circuit characteristics of the unit cell. For this purpose, two cooling conditions are studied which have been recently discussed in literature, namely surface cooling[54,55] and tab cooling.[55,56] By accounting for the same short circuit condition for all cells representing a low external short circuit resistance (i.e. applying the same boundary condition approaching a cell voltage of 0 V), a most comparable evaluation of the interaction of cell format, size, and cooling condition can be achieved. Another approach would be to apply the same short circuit resistance to all cells implying lower overall current densities with increasing cell size. This would require an adaption of area specific short circuit resistances applied to the unit cell for each cell format and size in order
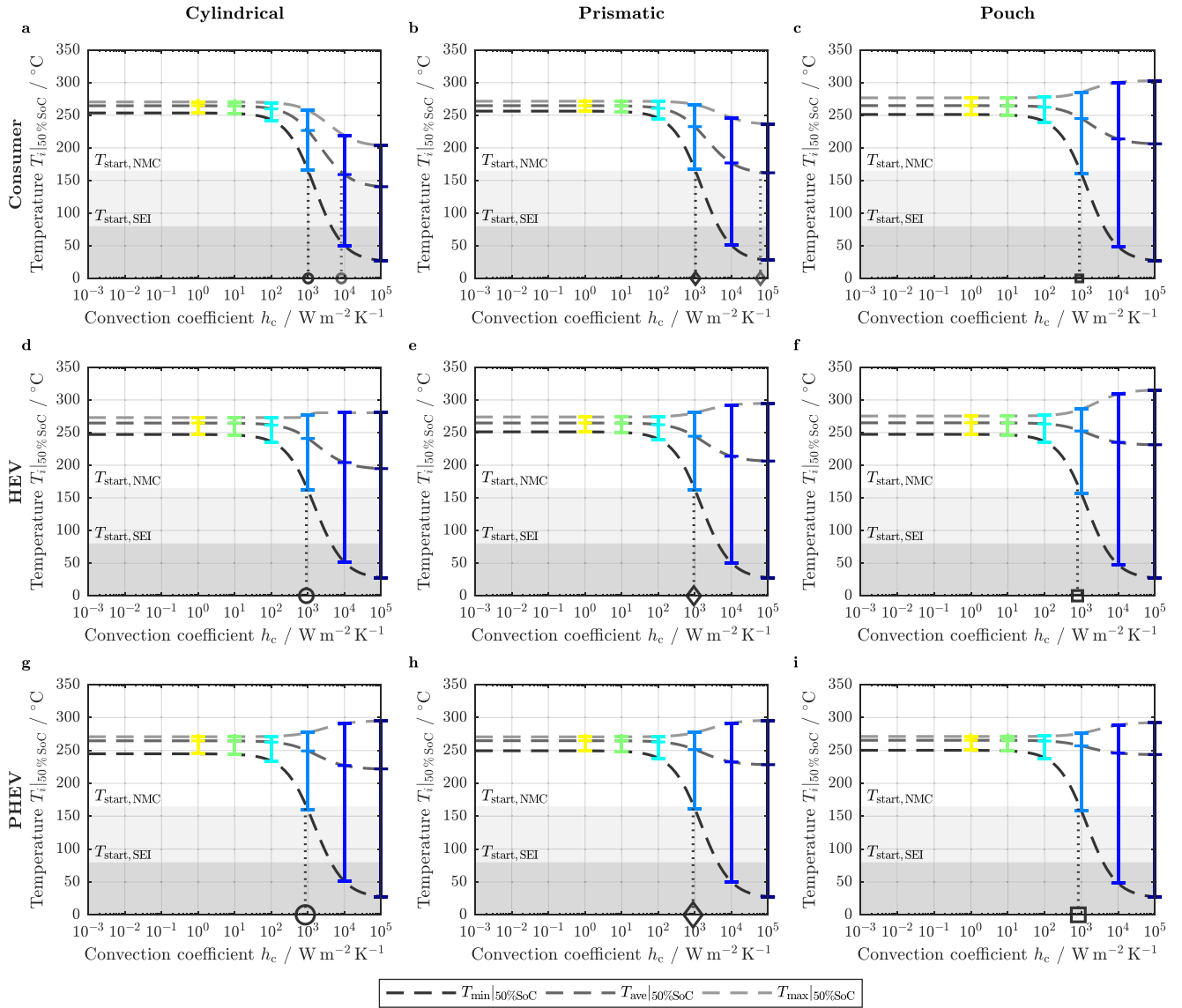
Figure 8. Predicted minimum, average, and maximum temperature of the studied cell formats and sizes in accordance with Table II for consumer-sized (top: a, b, and c), HEV-sized (middle horizontal: d, e, and f), and PHEV-sized (bottom: g, h, and i) cylindrical (left: a, d, and g), prismatic (middle vertical: b, e, and h), and pouch-type cells (right: c, f, and i) at an average cell SoC of 50% applying a tab cooling with convection coefficients h_c ranging from 1 W m^{-2} K^{-1} to 10^5 W m^{-2} K^{-1} and a constant coolant temperature of 25°C as a function of h_c. The vertical dotted lines and markers indicate a cooling below the threshold temperature $T_{\text{start, NMC}}$ for each individual temperatures. Colors are chosen in accordance with Figs. 2, 4, and 6.

to allow for a straightforward comparison to the electrochemical unit cell.

The short circuit behavior of an HEV-sized prismatic cell is exemplarily shown in Fig. 6 applying a surface cooling with various convection coefficients at a coolant temperature of 25°C. When comparing Fig. 6 to Fig. 2, a strong difference between the thermally well-connected unit cell and the geometrically restricted prismatic cell becomes apparent. Whilst the unit cell's temperature cannot only be maintained below the temperature threshold of exothermic side reactions but can even be operated under isothermal conditions if the chosen cooling condition is sufficiently strong, the HEV-sized prismatic cell cannot be cooled to the same extent. This implies that even under conditions representing a direct phase change at the surface of the wound electrode configuration, keeping the cell's average temperature below $T_{\text{start, NMC}}$ throughout the entire short circuit duration is not possible, let alone the cell's maximum temperature. Hence, exothermic side reactions involving the positive electrode which may result in cell thermal runaway must be expected to occur. The rea-

son for this temperature increase can be found in a reduced effective cooling rate $\dot{q}_{c,\text{eff}}$ (W m^{-2} K^{-1}) with respect to the coated electrode area (see Figs. 6b and 6f):

$$\dot{q}_{c,\text{eff}} = \dot{q}_c \cdot \frac{A_{\text{surf/tab}}}{A_{\text{ele}}} = \dot{q}_c \cdot \frac{A_{\text{surf/tab}}}{2 \cdot w_{\text{ele}} \cdot h_{\text{ele}}} \qquad [1]$$

whereas A_{surf} or A_{tab} represent the cooled area of the jelly roll or electrode stack, depending on the applied cooling strategy, and A_{ele} describes the double-sided electrode area of the investigated cell. This effective cooling rate is partly reduced by over a magnitude compared to the electrochemical unit cell (see Figs. 2b and 2f) which is based on the limited surface area available for cooling in the first place, and a reduced surface temperature resulting from an increased thermal resistivity in the second place. These two effects, which are related to geometric and thermophysical properties of the cell and its jelly roll or electrode stack, both directly affect the overall cooling performance:

$$\dot{Q}_c = h_c \cdot A_{\text{surf/tab}} \cdot (T_{\text{surf/tab}} - T_c) \qquad [2]$$
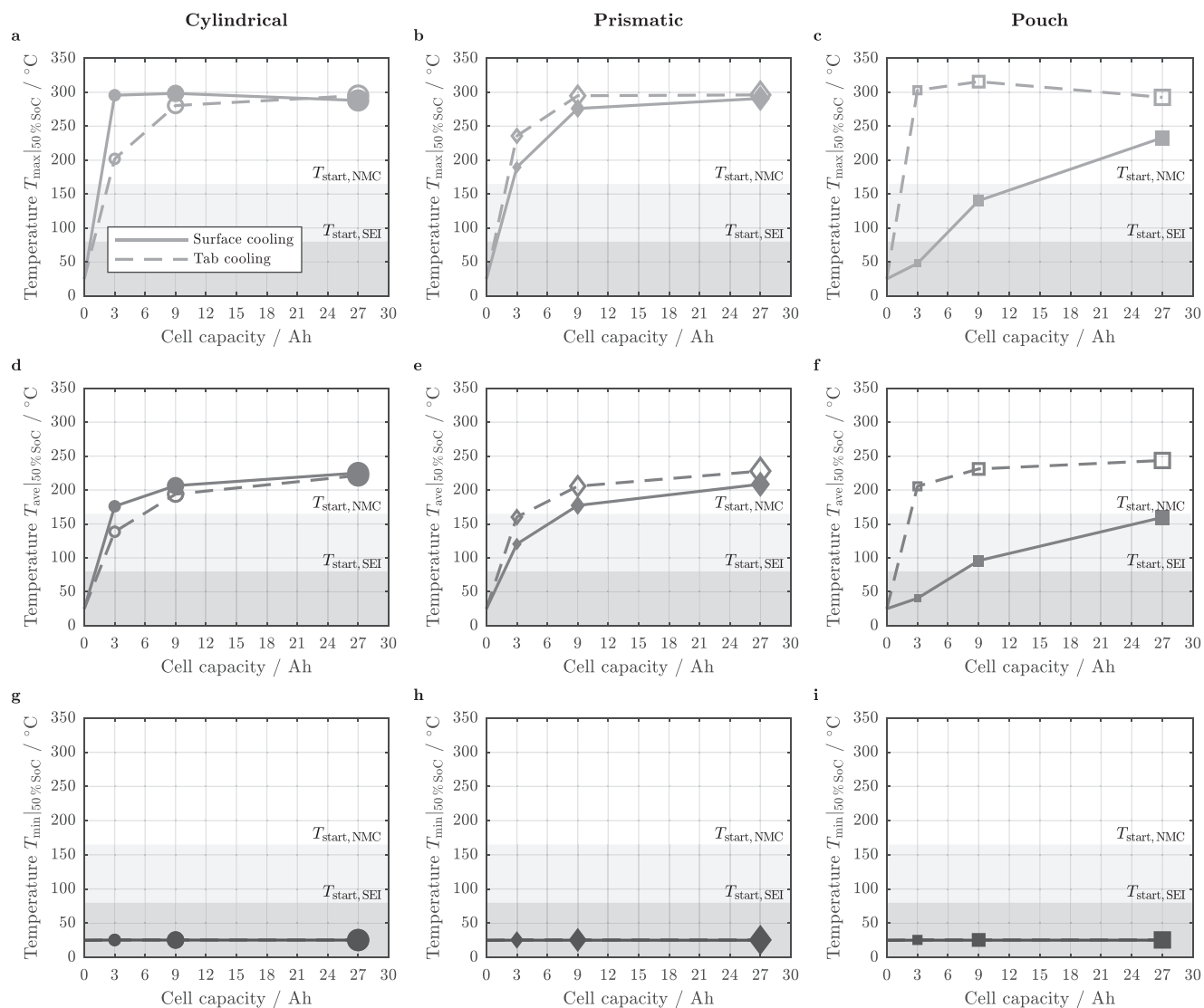
Figure 9. Approximated maximum (top: a, b, and c), average (middle horizontal: d, e, and f), and minimum cell temperature (bottom: g, h, and i) at maximum convective cooling (i.e. h_c approaching ∞) and a constant coolant temperature of 25°C of the studied cell formats and sizes in accordance with Table II for cylindrical (left: a, d, and g), prismatic (middle vertical: b, e, and h), and pouch-type cells (right: c, f, and i) at an average cell SoC of 50% applying a both surface and tab cooling as a function of cell capacity.

whereas T_{surf} or T_{tab} represent the local temperature of the cooled area depending on the applied cooling strategy and T_c describes the coolant temperature. The limited effect of the applied cooling conditions results in an almost unaffected short circuit behavior with similar C-rates and little variation in short circuit duration (see Figs. 6a, 6c, and 6e).

When studying the cell temperature at an average SoC of 50% in accordance with Fig. 4, the effect of cell format and size becomes obvious for both surface cooling (see Fig. 7) and tab cooling (see Fig. 8).

With the geometrical restrictions of the studied cells, considerable inhomogeneities are provoked which generally become more pronounced with growing cell size and increased cooling performance represented by larger convection coefficients h_c. However, even at low cooling rates approaching natural convection (ca. 1 W m^{-2} K^{-1}), a considerable difference between the minimum, average, and maximum cell temperature can be observed at 50% SoC, which can also not be ruled out completely even under adiabatic conditions (i.e. 0 W m^{-2} K^{-1}, not shown here). This can be explained with the polarization along the electrodes during operation involving an inhomogeneous

current density distribution and, consequently, spatially varying heat generation rates, temperatures, cell polarization, and so forth building up throughout discharge. The impact of the chosen cell format and size as well as the applied cooling strategy becomes obvious when comparing the characteristics shown in Fig. 7 and Fig. 8 to the behavior of the unit cell shown in Fig. 4 as a function of convection coefficient. Whilst the minimum temperature can be maintained below $T_{start, NMC}$ for all cells with the chosen range of convection coefficients, the average and especially the maximum cell temperature T_{ave} and T_{max} can only be controlled for smaller and thinner cells.

This can be explained with a relatively large surface area and a limited resistance for heat conduction. With the chosen model assumptions, only surface cooled pouch-type cells of consumer and HEV size can be maintained below $T_{start, NMC}$ at 50% SoC. Whilst the average temperature of consumer-sized prismatic cells and PHEV-sized pouch-type cells can be physically reduced below this threshold, by applying a surface cooling, all other cell sizes and formats cannot be maintained below $T_{start, NMC}$ for both T_{ave} and T_{max}. Due to the larger electrode length and reduced electrode height of cylindrical cells in comparison to prismatic and pouch-type cells, a slightly reversed pic-

ture can be observed between these three cell formats when applying a tab cooling, which allows the average cell temperature to be kept below $T_{\text{start, NMC}}$ for consumer-sized cylindrical and prismatic cells at convection coefficients exceeding 10000 W m^{-2} K^{-1}. All other studied combinations of format and size cannot be maintained below this threshold on average.

It becomes furthermore apparent that besides limitations of the applied convective cooling with 100000 W m^{-2} K^{-1} marking the somewhat upper range of physically possible heat transfer coefficients, both cell format and size also geometrically limit the heat that can be extracted from the cell. Whilst the temperature of the unit cell can be maintained isothermal if the cooling is chosen sufficiently strong, this seemingly cannot be achieved for larger sized cells showing an asymptotic approach of higher temperature levels for both average and maximum cell temperature. Furthermore, even though the average temperature is generally reduced with increasing convection coefficients, the maximum cell temperature at 50% SoC seems to partly increase depending on the cell's format and size combined with the chosen cooling strategy. This appears to be the case for all conditions in which a cooling of the cell's average temperature below $T_{\text{start, NMC}}$ is not possible. This effect can be only explained by vast inhomogeneities within the cell triggered by the temperature distribution fostering large local current densities and heat generation rates at higher temperature regions (e.g. center of the jelly roll or electrode stack), paired with a limited cooling capability which predominantly affects regions where comparably low currents and heat generation rates can be observed (e.g. surface near regions of the jelly roll or electrode stack). The temperature at maximum convective cooling (i.e. h_c approaching ∞) can be estimated by fitting the data shown in Fig. 7 and Fig. 8 via a hyperbolic tangent function (solid and dashed lines in Figs. 7 and Fig. 8), which is shown in Fig. 9 for the minimum, average, and maximum cell temperature. Following this approach, a critical cell size for each format and cooling condition can be derived which still allows for a complete cooling of the cell below a critical threshold temper-

ature. Only surface cooled pouch-type cells can still be maintained below $T_{\text{start, NMC}}$ in terms of average and maximum temperatures for cell sizes beyond the considered HEV size. For all other combinations of cell format and cooling condition, only a cell size below the studied 3 Ah consumer size could possibly be kept below this temperature threshold at the applied short circuit condition.

Furthermore, the graphic representation showing the cooling performance in Fig. 9 allows a direct comparison of the effectiveness of surface cooling and tab cooling. Whilst the cylindrical cell can be physically maintained at lower temperatures via tab cooling, both prismatic and especially pouch-type cells can be cooled more efficiently via surface cooling. The general cooling capability of the three studied cell formats increases from cylindrical, to prismatic, and pouch-type cell with a stronger dependency on the applied cooling strategy (see spread between solid and dashed lines in Figs. 9a to 9f).

By further comparing the convection coefficients at which the minimum cell temperature falls below $T_{\text{start, NMC}}$ to the convection coefficient that needs to be applied to the unit cell for a cooling below this threshold, the loss in cooling efficiency due to geometrical restrictions becomes apparent (see Fig. 10). Whilst a convection coefficient of just under 20 W m^{-2} K^{-1} is sufficient for cooling the whole unit cell below $T_{\text{start, NMC}}$ at 50% SoC, a range between 150 W m^{-2} K^{-1} and 180 W m^{-2} K^{-1} must be applied for the surface cooling (see Fig. 10a) which increases toward 800 W m^{-2} K^{-1} and beyond 1000 W m^{-2} K^{-1} (see Fig. 10b) for the tab cooling, in order to reduce at least the cell's minimum temperature below this value depending the format and size of the cells. This increase by a factor of approximately 10 to 50 for the surface and tab cooling compared to the unit cell underlines not only the geometric restrictions of cooling larger sized cells but also reveals a superior cooling capability of surface cooling compared to tab cooling for the studied cells. However, this representation does not allow an easy distinction between the cooling capabilities of different cell formats and sizes.
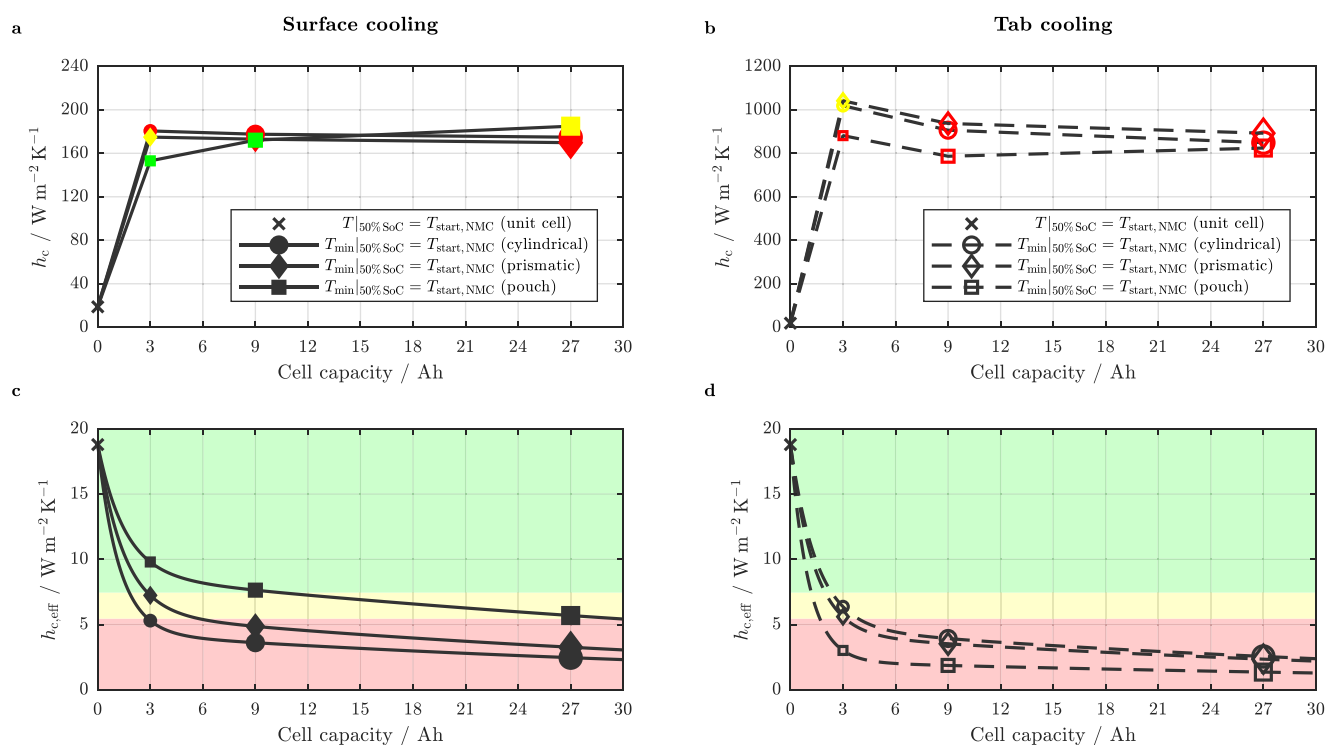
Figure 10. Approximated convection coefficients h_c (top: a and b) and approximated effective convection coefficients $h_{c,\text{eff}}$ (bottom: c and d) beyond which the temperature of the electrochemical unit cell and the minimum temperature of the studied cell formats and sizes (see Table II) fall below $T_{\text{start, NMC}}$ at an average cell SoC of 50% applying both a surface (left: a and c) and tab cooling (right: b and d) as a function of cell capacity. Green markers and area indicate a sufficient cooling to reduce both $T_{\text{ave}}|_{50\% \text{Soc}}$ and $T_{\text{max}}|_{50\% \text{Soc}}$ below $T_{\text{start, NMC}}$, yellow markers and area indicate a cooling of $T_{\text{ave}}|_{50\% \text{Soc}}$ below this threshold, and red markers and area indicate an insufficient cooling with both $T_{\text{ave}}|_{50\% \text{Soc}}$ and $T_{\text{max}}|_{50\% \text{Soc}}$ exceeding $T_{\text{start, NMC}}$.

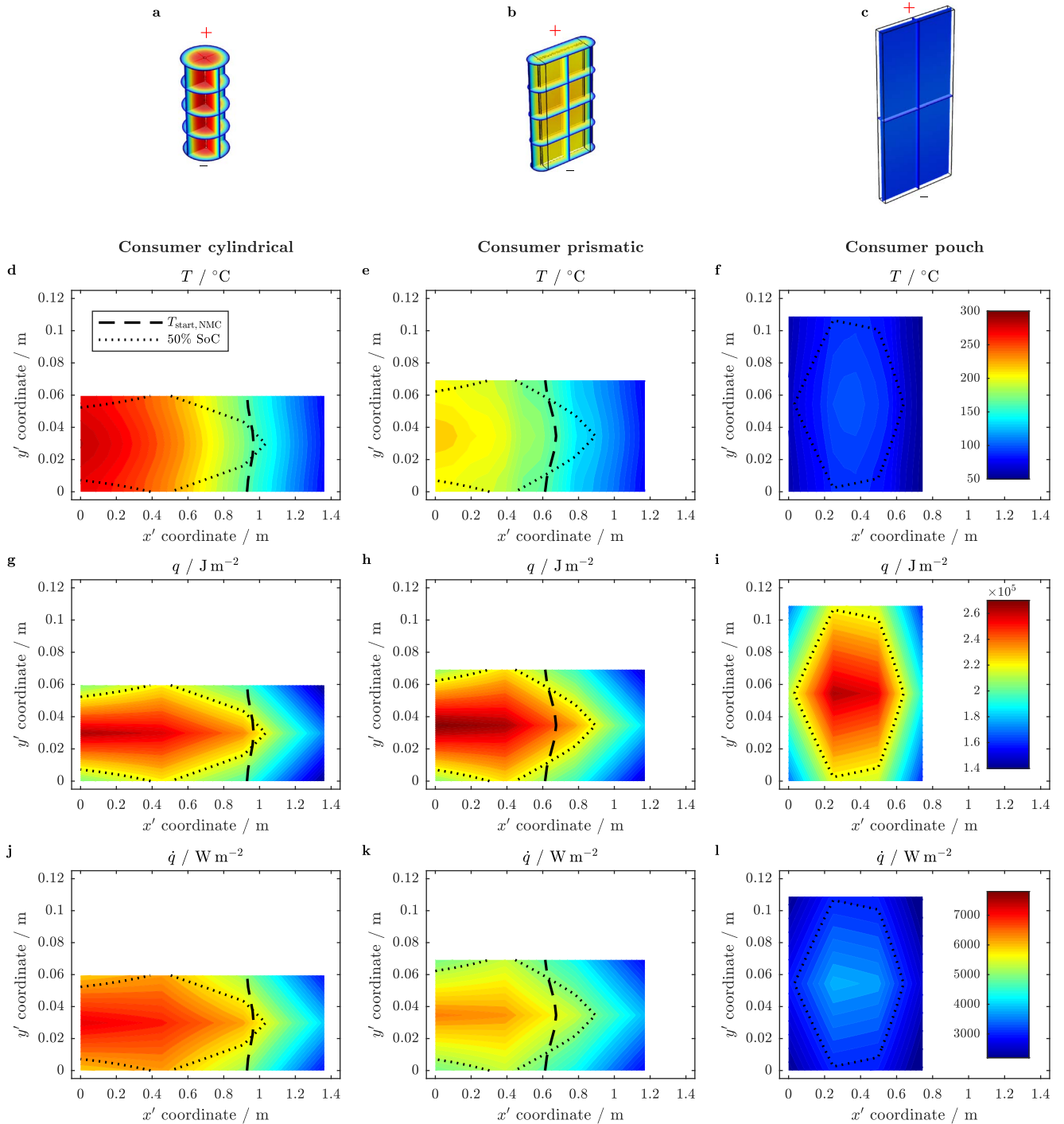**Figure 11.** Predicted cell temperature for the 3D geometry of the jelly roll or electrode stack (a, b, and c) and for the mapped 2D representation along the electrodes with $x' = 0$ marking the beginning of the jelly roll or electrode stack (d, e, and f) based on the accumulated area specific heat q (g, h, and i) and the superimposed heat dissipation at an average SoC of 50% together with the area specific heat generation rate $\dot{q}$ (j, k, and l) for the cylindrical (left: a, d, g, and j), prismatic (middle: b, e, h, and k), and pouch-type consumer sized cells (right: c, f, i, and l) at a surface cooling of 1000 W m^{-2} K^{-1} and 25°C. The dashed and dotted lines indicate the threshold temperature $T_{\text{start, NMC}}$ and 50% SoC, respectively. The color range shown in f applies to all temperature data (a to f).

By further relating the cooled area A_{surf} or A_{tab} to the overall (double-sided) electrode area A_{ele} (see Table II), an effective cooling coefficient $h_{\text{c, eff}}$ can be derived in analogy to Eq. 1:

$$h_{\text{c, eff}} = h_{\text{c}} \cdot \frac{A_{\text{surf/tab}}}{A_{\text{ele}}} = h_{\text{c}} \cdot \frac{A_{\text{surf/tab}}}{2 \cdot w_{\text{ele}} \cdot h_{\text{ele}}} \quad [3]$$

Whilst $h_{\text{c, eff}} = h_{\text{c}}$ for the unit cell, the effective cooling coefficient strongly decreases for the surface and tab cooling of larger sized cells (compare Figs. 10a and 10b to 10c and 10d). When further rating a cell and cooling condition that allows for a cooling of both a cell's average and maximum temperature below $T_{\text{start, NMC}}$ at 50% SoC as uncritical (see green markers and area in Fig. 10) and an exceeding of both average and maximum temperatures as critical (see red markers

and area in Fig. 10), the combination of cell format, size, and applied cooling strategy can be assessed (see Figs. 10c and 10d). Hence, a cell and cooling condition resulting in an effective convection coefficient below 5.5 W m^{-2} K^{-1} at which the minimum cell temperature falls below $T_{start, NMC}$ can be regarded as critical (see red markers and area in Figs. 10c and 10d). An effective cooling coefficient beyond 7.5 W m^{-2} K^{-1} results in an uncritical behavior (see green markers and area in Figs. 10c and 10d). The range in between these two values, which

is characterized by an average temperature below and a maximum temperature beyond $T_{start, NMC}$ at 50% SoC, marks a transition which needs to be considered more closely in terms of local temperatures and SoCs in order to be able to evaluate the likelihood of exothermic side reactions that may result in a cell thermal runaway (see yellow markers and area in Figs. 10c and 10d).

Such evaluation is exemplarily shown in Fig. 11 and Fig. 12 for consumer-sized cells with an applied surface cooling of $h_c = 1000$ W

Figure 12. Predicted cell temperature for the 3D geometry of the jelly roll or electrode stack (a, b, and c) in accordance with Fig. 11 together with the corresponding local cell potential E (d, e, and f), cell SoC (g, h, and i), and the through-plane current density i_{p2D} (j, k, and l) at an average SoC of 50% for the cylindrical (left: a, d, g, and j), prismatic (middle: b, e, h, and k), and pouch-type consumer sized cells (right: c, f, i, and l) at a surface cooling of 1000 W m^{-2} K^{-1} and 25°C. The dashed and dotted lines indicate the threshold temperature $T_{start, NMC}$ and 50% SoC, respectively.
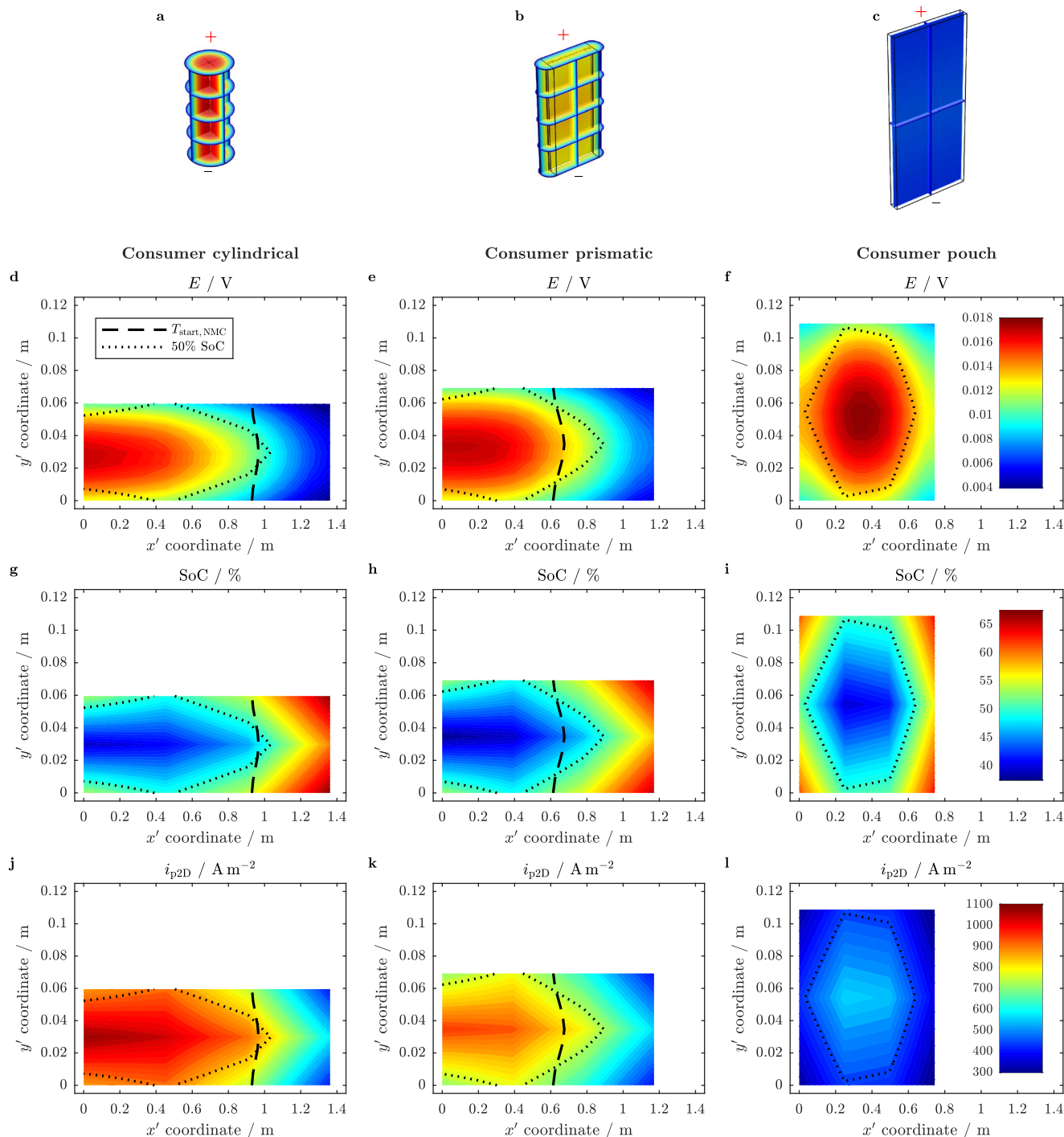
Figure 13. Predicted cell temperature for the 3D geometry of the jelly roll or electrode stack (a, b, and c) and for the mapped 2D representation (d, e, and f) based on the accumulated area specific heat q (g, h, and i) and the superimposed heat dissipation at an average SoC of 50% together with the area specific heat generation rate $\dot{q}$ (j, k, and l) for the cylindrical (left: a, d, g, and j), prismatic (middle: b, e, h, and k), and pouch-type consumer sized cells (right: c, f, i, and l) at a tab cooling of 1000 W m^{-2} K^{-1} and 25°C. The dashed and dotted lines indicate the threshold temperature $T_{\text{start, NMC}}$ and 50% SoC, respectively. The color range shown in f applies to all temperature data (a to f).

m^{-2} K^{-1} at 50% SoC. The derived distribution in temperature T (see Figs. 11a to 11f) is based on the accumulated area specific heat q (J m^{-2}) shown in Figs. 11g, 11h, and 11i and the underlying area specific heat generation rate $\dot{q}$ (W m^{-2}) shown in Figs. 11j, 11k, and 11l. As can be seen from Fig. 11, large temperature gradients form especially for the cylindrical and prismatic cell compared to the pouch-

type cell which is also shown in Fig. 7. With the chosen model discretization of the coupled p2D physical-chemical/2D electrical electrode model (i.e. eight p2D models per Ah for all presented models), a coarser distribution in accumulated heat (see Figs. 11g, 11h, and 11i) and underlying heat generation rate (see Figs. 11j, 11k, and 11l) can be observed compared to the calculated 3D (see Fig. 11a, 11b,
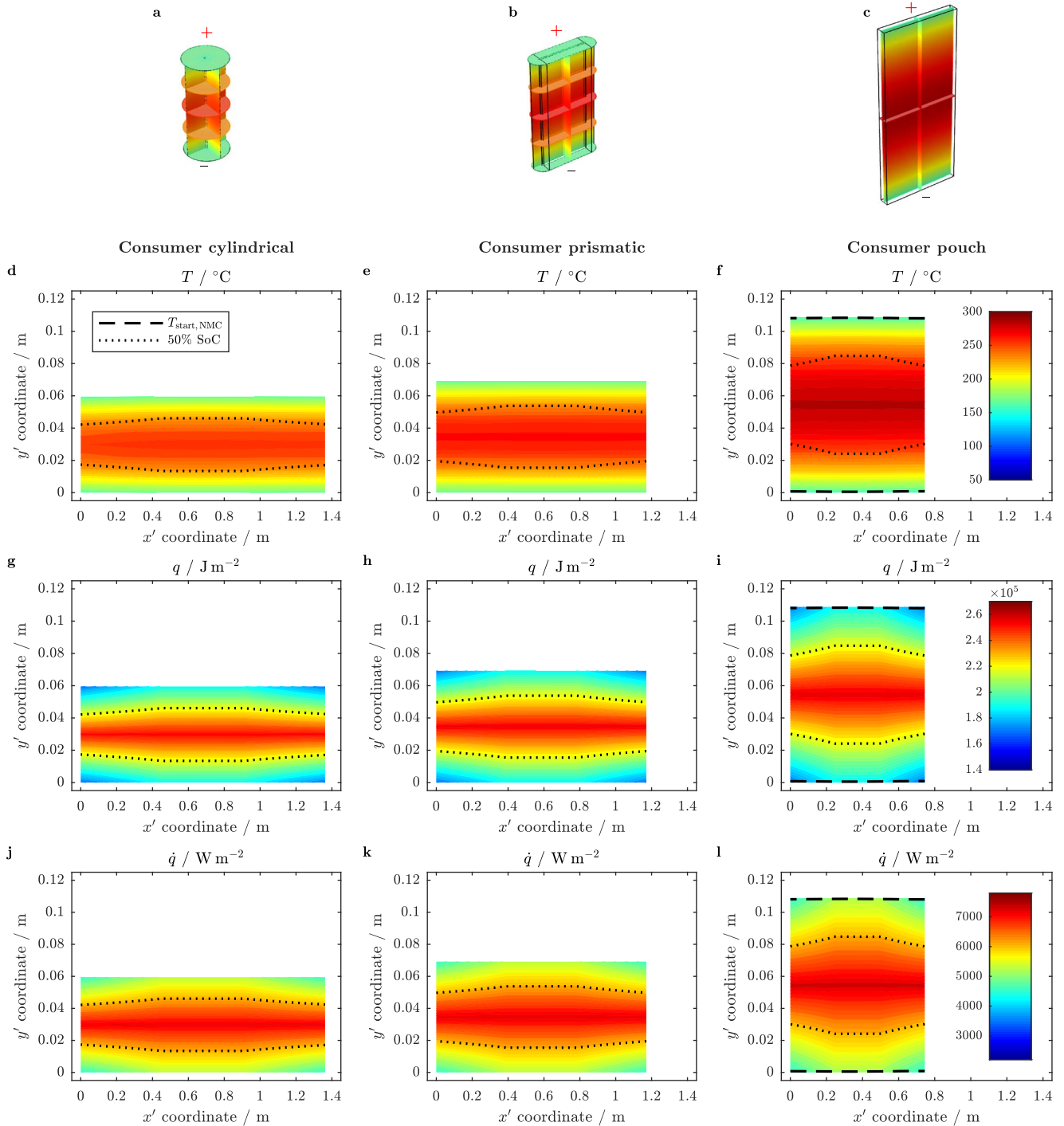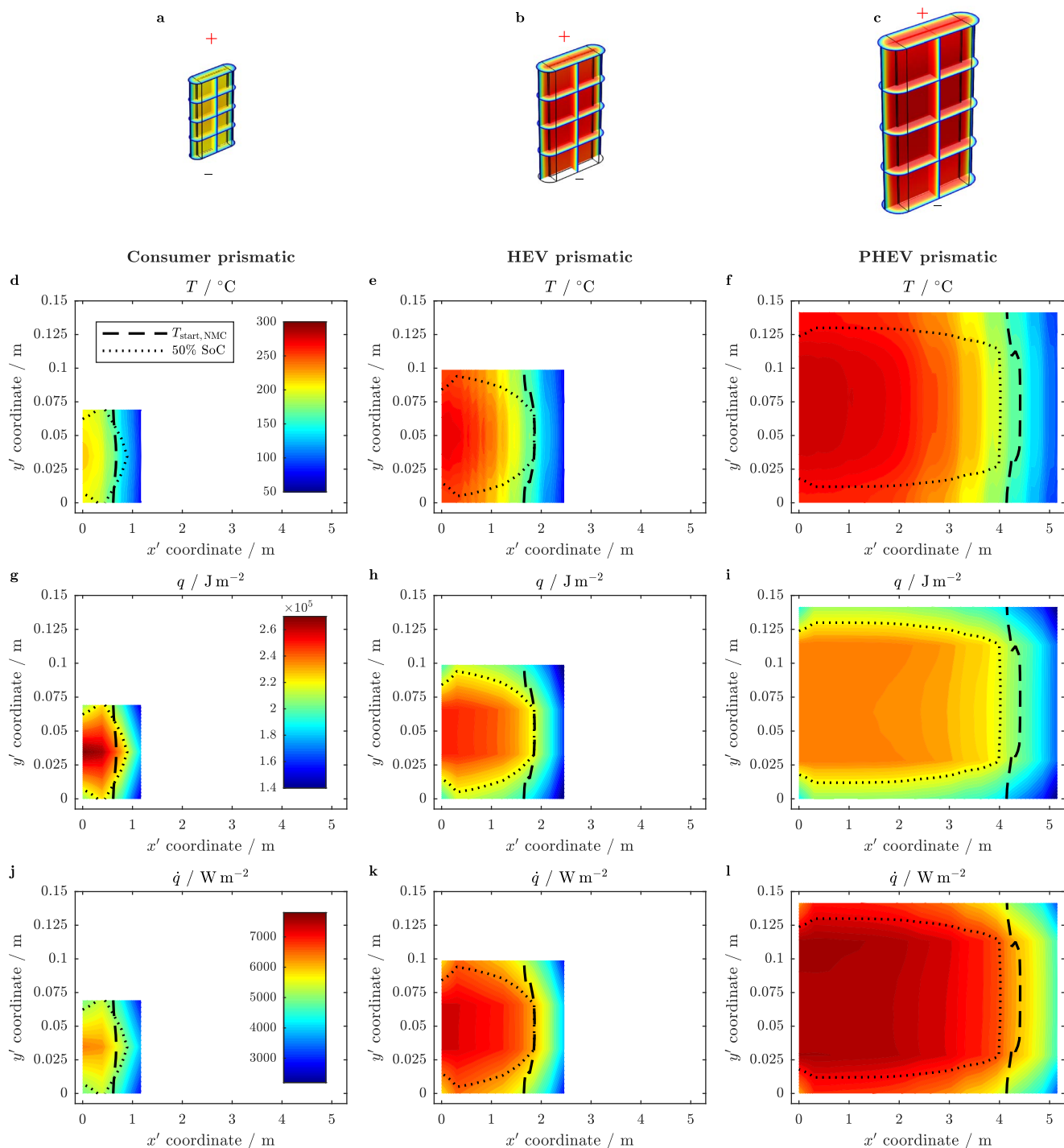
Figure 14. Predicted cell temperature for the 3D geometry of the jelly roll or electrode stack (a, b, and c) and for the mapped 2D representation along the electrodes (d, e, and f) based on the accumulated area specific heat q (g, h, and i) and the superimposed heat dissipation at an average SoC of 50% together with the area specific heat generation rate $\dot{q}$ (j, k, and l) for the consumer-sized (left: a, d, g, and j), HEV-sized (middle: b, e, h, and k), and PHEV-sized prismatic cells (right: c, f, i, and l) at a surface cooling of 1000 W m^{-2} K^{-1} and 25°C. The dashed and dotted lines indicate the threshold temperature $T_{\text{start, NMC}}$ and 50% SoC, respectively. The color range shown in f applies to all temperature data (a to f).

and 11c) and mapped 2D temperature distribution (see Figs. 11d, 11e, and 11f).

With the limited penetration depth of the applied cooling strategy, about two-thirds of the electrode width ranges above $T_{\text{start, NMC}}$ for the consumer-sized cylindrical cell, whereas this ratio is reduced to half of the electrode width for the prismatic cell. The pouch-type cell ranges

completely below this threshold due to a comparably effective penetration of the cooling strategy (see dashed line in Fig. 11). When looking into the spatial distribution of electrochemical and electrical variables, such as local cell potential E (V, see Figs. 12d, 12e, and 12f), SoC (see Figs. 12g, 12h, and 12i), and through-plane current density i_{p2D} (A m^{-2}, see Figs. 12j, 12k, and 12l), it becomes obvious that the

current follows the temperature, resulting in the lowest SoCs at regions with the highest cell and electrode temperatures. With the presented cell formats and sizes, the 50% SoC boundary does not completely fill the area marked by the $T_{\text{start, NMC}}$ threshold for both cylindrical and prismatic cell types (compare dotted line to dashed line in Fig. 11 and Fig. 12). This would most likely result in considerable exothermic side reactions involving the positive electrode especially at tab-near regions within the cell's center at this very moment of the short circuit. With the average temperature of the prismatic cell ranging below the temperature of the cylindrical cell, the area which is affected by a potentially critical combination of temperature and SoC is smaller for the prismatic cell compared to the cylindrical cell. The consumer-sized pouch-type cell shows overall lower temperatures than $T_{\text{start, NMC}}$ at 50% SoC with a slightly unsymmetrical SoC distribution along the electrode width, which can be explained with the applied folding pattern and scaling of the chosen representative cell format from PHEV to HEV and consumer size. This involves an odd number of electrode layers which are z-folded to form the HEV and cylindrical cells based on the scaling from the PHEV1/BEV1 pouch-type cell whilst keeping the aspect ratio constant. As a result, the thermal representation of the cylindrical and HEV-sized electrode stack includes regions at the very end of the electrodes which are not heated. This provokes a slightly unsymmetrical temperature distribution, which affects the current density distribution and, hence, heat generation rate as shown in Fig. 11 and Fig. 12. By applying a tab cooling of 1000 W m^{-2} K^{-1} to the considered consumer-sized cells, all three cell formats surpass $T_{\text{start, NMC}}$ throughout almost the entire electrode area (see Fig. 13) at 50% SoC with the largest temperature gradients forming for the pouch-type cell, showing the highest maximum temperature among the three formats and also the lowest minimum temperature bordering $T_{\text{start, NMC}}$ directly at the tab region (see dashed line in Fig. 13f).

With the SoC inversely following the temperature distribution, showing the lowest SoCs at approximately half the electrode height (see dotted line in Fig. 13), an initiation of exothermic side reactions within the cell's center with a reaction front moving toward the tabs is likely, as the SoC reduction is seemingly not as fast as the temperature increase leading to potentially critical temperature and SoC combinations throughout the short circuit. With increasing cell size, the outpacing of a temperature increase beyond $T_{\text{start, NMC}}$ compared to an SoC decrease toward 50% or less becomes more pronounced which is exemplarily shown for the prismatic cell at a surface cooling of 1000 W m^{-2} K^{-1} (see Fig. 14). Despite the larger amount of area specific heat q accumulated throughout the short circuit within the cell's center of the consumer-sized prismatic cell compared to its HEV-sized and PHEV-sized representatives (see Figs. 14g to 14l), lower maximum temperatures can be observed which supports a superior cooling performance of smaller-sized cells due to a lower thermal resistivity.

Conclusions

The presented model helps to shed light on the short circuit performance of Li-ion cells of various formats and sizes under varying cooling conditions. With the suggested mapping procedure, exchanging temperature and heat generation rate between the 3D thermal model of the cell's jelly roll or electrode stack and the 2D electrical model of the planar electrodes, not only consumer-sized Li-ion cells but also larger, automotive cells can be described under extreme conditions such as short circuits, which demand a considerably detailed discretization especially for the p2D physical-chemical models between the two current collector foils. Whilst a thermally well-connected electrochemical unit cell can be rather easily maintained below a temperature threshold triggering exothermic side reactions and can be further shorted under quasi-isothermal operation as previously demonstrated,[14] larger sized cells pose a significant challenge to be maintained within a safe operating window, defined by the cell's local temperature and SoC. The limited heat dissipation throughout the cell's jelly roll or electrode stack make a sufficient cooling almost impossible for the chosen cell

formats and sizes as well as the applied cooling conditions in case a short circuit is maintained. Even though the minimum cell temperature can be physically reduced to uncritical temperature levels, the average and maximum cell temperature within the cell's center can partly not be controlled, even though a physically maximized convective cooling is applied at moderate coolant temperatures. On the one hand, a reduced coolant temperature can enhance the cooling capability of the cooling system which might be able to push the cell's average and maximum temperature to lower values. On the other hand, a limited cell size combined with a maximized cooled surface area and minimized thermal resistivity improves the cooling capability of the cell itself. When applied and combined effectively, both of these measures can increase the likelihood of preventing cell thermal runaway as a result of external short circuits. Furthermore, alternative approaches focusing on altering the electrode design such as increasing the electrode loading by reducing the porosity, might intrinsically limit the short circuit current due to increased liquid phase limitations.[15,57,58] Such an approach, will be more closely investigated by our group in future. The question of an ideal cell design allowing for a maximum level of safety whilst guaranteeing the required energy and power characteristics, however, cannot be answered with such a cell model on its own. This requires further considerations of safety mechanisms included in the various cell designs and restrictions arising from module and pack integration.

The suggested criteria, outlining a critical temperature increase beyond the thermal stability window of the cell's active and passive components combined with a critical SoC threshold, need to be more thoroughly studied in future in order to be able to derive a safe operating window for various material combinations. This however, requires experimental data and models which are capable of reliably describing thermal decomposition reactions as a function of cell SoC or degree of lithiation within the active material particles, which can only be scarcely found in literature so far.[46] Such considerations need to be further evaluated in the context of aging which not only affects the reactivity of the individual exothermic side reactions,[46,59] but also increases the cell's electrical and electrochemical resistivity affecting short circuit currents and heat generation rates. Based on the presented difficulties of maintaining a cell within a safe temperature and SoC window during short circuit events, especially with increasing cell size, cell thermal runaway must be more thoroughly described including the cell's interactions with its surroundings (e.g. venting) in order to evaluate possibilities to design batteries which can tolerate cell thermal runaway without propagation to neighboring cells or modules.

With the aid of the presented model, also local or internal short circuits can be described which will be the focus of upcoming work of the group. Besides these activities, validating electro-thermal models under both normal operation and abusive conditions is also part of future activities which will allow for further improvement in the quality of the discussed modeling approaches.

Appendix

$$\frac{dE_{\text{eq, neg}}}{dT} =$$

$$\frac{-3.8149 \times 10^{-4} x^5 + 1.058 \times 10^{-3} x^4 - 1.1235 \times 10^{-3} x^3 + 5.5727 \times 10^{-4} x^2 - 1.242 \times 10^{-4} x + 9.0095 \times 10^{-6}}{x^5 - 2.9967 x^4 + 3.2192 x^3 - 1.4066 x^2 + 1.8475 \times 10^{-1} x + 1.3198 \times 10^{-2}}$$

[A1]

Table A1. Model parameters for the physical-chemical model of the electrochemical unit cell (p2D-EC), the electrical model of the electrode layers (2D-E), and the thermal model of the jelly roll or electrode stack (3D-T). Model parameters of the p2D-EC model were chosen in accordance with Ref. 15.

Description	Symbol	Unit	Negative electrode Cu (cc) & LiC (neg)	Separator polyolefin (sep)	Positive electrode NMC-111 (pos) & Al (cc)
p2D-EC model parameters					
Equilibrium potential[m,15]	$E_{\mathrm{eq},i}$	V	see Ref. 15	n/a	see Ref. 15
Entropic coefficient[l,64,65]	$\frac{dE_{\mathrm{eq},i}}{dT}$	V K^{-1}	fitted,[64] see Eq. A1	n/a	fitted,[65] see Eq. A2
Anodic and cathodic reaction rate constant[l,5]	$k_{\mathrm{a/c},i}$	m s^{-1}	2×10^{-11}	n/a	2×10^{-11}
Anodic and cathodic charge transfer coefficient[e]	$\alpha_{\mathrm{a/c},i}$	-	0.5	n/a	0.5
Film resistance[l,16]	R_{film}	Ω m^{-2}	0.0035	n/a	0
Maximum solid phase concentration[c]	$c_{\mathrm{s,max},i}$	mol m^{-3}	29862	n/a	49242
Solid phase electronic conductivity[e]	$\sigma_{\mathrm{s},i}$	S m^{-1}	100	n/a	10
Solid phase diffusion coefficient[e,15]	$D_{\mathrm{s},i}$	m^2 s^{-1}	fitted,[15] see Eq. A3	n/a	fitted,[15] see Eq. A4
Liquid phase ionic conductivity[l,47]	κ_{l}	S m^{-1}		modified from Ref. 47, see Eq. A5	
Liquid phase diffusion coefficient[l,47]	D_{l}	m^2 s^{-1}		modified from Ref. 47, see Eq. A6	
Liquid phase transference number[l,47]	t_{+}	-		0.38	
Liquid phase thermodynamic factor[l,47]	TDF	-		modified from Ref. 47, see Eq. A7	
Particle size (D50)[m]	$R_{\mathrm{p},i}$	µm	11	n/a	7
Coating and separator thickness[m]	l_i	µm	67	25	79
Porosity[c]	$\epsilon_{\mathrm{l},i}$	%	51.3	50	48.7
Active material volume fraction[c]	$\epsilon_{\mathrm{s},i}$	%	46.4	n/a	36.4
Tortuosity[e]	τ_i	-	$\epsilon_{\mathrm{l,neg}}^{-1.8}$	$\epsilon_{\mathrm{l,sep}}^{-1.8}$	$\epsilon_{\mathrm{l,pos}}^{-1.1}$
Stoichiometry[c] at $E_{\mathrm{eq,cell}} = 4.20$ V/SoC $= 100\%$	$\frac{c_{\mathrm{s}}}{c_{\mathrm{s,max},i}}$	%	76.6	n/a	42.5
$= 4.15$ V/SoC $= 96\%$			73.5		44.6
2D-E model parameters					
Current collector electronic conductivity[l,66,67]	$\sigma_{\mathrm{cc},i}$	S m^{-1}	see Eq. A8[66]	n/a	see Eq. A9[67]
Current collector thickness[e]	$l_{\mathrm{cc},i}$	µm	12	n/a	18
Electrode width[e]	$w_{\mathrm{ele},i}$	mm	see Table II	n/a	see Table II
Electrode height[e]	$h_{\mathrm{ele},i}$	mm	see Table II	n/a	see Table II

3D-T model parameters			Cu	LiC		NMC-111	Al
Density[l,68,69]	ρ_i	kg m^{-3}	8950[68]	1347.33[69]	1008.98[69]	2328.5[69]	2710[68]
Specific heat capacity[l,69]	$c_{p,i}$	J kg^{-1} K^{-1}	385	1437.4	1978.16	1269.21	903
Thermal conductivity[l,69]	λ_i	W m^{-1} K^{-1}	398	1.04	0.3344	1.58	238
Jelly roll/electrode stack width[e]	$w_{\mathrm{jelly/stack}}$	mm			see Table II		
Jelly roll/electrode stack height[e]	$h_{\mathrm{jelly/stack}}$	mm			see Table II		
Jelly roll/electrode stack thickness[e]	$d_{\mathrm{jelly/stack}}$	mm			see Table II		
Electrode layer thickness[c]	l_{layer}	µm			$l_{\mathrm{cc,neg}} + 2 \cdot (l_{\mathrm{neg}} + l_{\mathrm{sep}} + l_{\mathrm{pos}}) + l_{\mathrm{cc,pos}} = 372$		
Electrode layer density[c]	ρ_{layer}	kg m^{-3}			$\frac{\sum_i l_i \cdot \rho_i}{l_{\mathrm{layer}}} = 2029.77$		
Electrode layer specific heat capacity[c]	$c_{p,\mathrm{layer}}$	J kg^{-1} K^{-1}			$\frac{\sum_i l_i \cdot \rho_i \cdot c_{p,i}}{l_{\mathrm{layer}} \cdot \rho_{\mathrm{layer}}} = 1207.37$		
Electrode layer thermal conductivity (through-plane)[c]	$\lambda_{\perp}$	W m^{-1} K^{-1}			$\left(\frac{1}{l_{\mathrm{layer}}} \cdot \sum_i \frac{l_i}{\lambda_i}\right)^{-1} = 0.9829$		
Electrode layer thermal conductivity (in-plane)[c]	$\lambda_{\parallel}$	W m^{-1} K^{-1}			$\frac{\sum_i l_i \cdot \lambda_i}{l_{\mathrm{layer}}} = 25.445$		

[c]calculated.
[e]estimated.
[l]literature.
[m]measured.

Table A2. Main variables, governing partial differential equations, and additional analytic expressions solved within each domain of the p2D physical-chemical model of the electrochemical unit cell as well as prevailing boundary conditions and derived quantities.

Description	Negative electrode (neg)	Separator (sep)	Positive electrode (pos)
Variables and mathematical operators			
	$c_l(x,t),\, c_s(x,r,t),\, \Phi_l(x,t),\, \Phi_s(x,t)$	$c_l(x,t),\, \Phi_l(x,t)$	$c_l(x,t),\, c_s(x,r,t),\, \Phi_l(x,t),\, \Phi_s(x,t)$
	$x \in [0;\, l_{\text{neg}}]$	$x \in [l_{\text{neg}};\, l_{\text{neg}}+l_{\text{sep}}]$	$x \in [l_{\text{neg}}+l_{\text{sep}};\, l_{\text{neg}}+l_{\text{sep}}+l_{\text{pos}}]$
	$r \in [0;\, r_{\text{p, neg}}]$		$r \in [0;\, r_{\text{p, pos}}]$
		$\nabla := \left(\frac{\partial}{\partial x}\right)$	
Governing partial differential equations			
Mass balance (liquid)	$\epsilon_{l,\text{neg}} \frac{\partial c_l}{\partial t} = \nabla(D_{l,\text{eff}} \nabla c_l) - \nabla\left(\frac{\mathbf{i}_l(1-t_+)}{F}\right)$	$\epsilon_{l,\text{sep}} \frac{\partial c_l}{\partial t} = \nabla(D_{l,\text{eff}} \nabla c_l)$	$\epsilon_{l,\text{pos}} \frac{\partial c_l}{\partial t} = \nabla(D_{l,\text{eff}} \nabla c_l) - \nabla\left(\frac{\mathbf{i}_l(1-t_+)}{F}\right)$
Mass balance (solid)	$\frac{\partial c_s}{\partial t} = \frac{1}{r^2}\frac{\partial}{\partial r}\left(D_{s,\text{neg}} r^2 \frac{\partial c_s}{\partial r}\right)$	n/a	$\frac{\partial c_s}{\partial t} = \frac{1}{r^2}\frac{\partial}{\partial r}\left(D_{s,\text{pos}} r^2 \frac{\partial c_s}{\partial r}\right)$
Ohm's law (liquid)		$\mathbf{i}_l = -\kappa_{l,\text{eff}} \nabla \Phi_l + \frac{2\kappa_{l,\text{eff}} RT}{F}(1-t_+)\left(1+\frac{\partial \ln f_\pm}{\partial \ln c_l}\right)\nabla \ln c_l$	
Ohm's law (solid)	$\mathbf{i}_s = -\sigma_{s,\text{eff}} \nabla \Phi_s$	n/a	$\mathbf{i}_s = -\sigma_{s,\text{eff}} \nabla \Phi_s$
Charge balance	$\nabla \mathbf{i}_l = -\nabla \mathbf{i}_s = \frac{3\epsilon_{s,\text{neg}}}{r_{\text{p, neg}}} i_n$	$\nabla \mathbf{i}_l = 0$	$\nabla \mathbf{i}_l = -\nabla \mathbf{i}_s = \frac{3\epsilon_{s,\text{pos}}}{r_{\text{p, pos}}} i_n$
Additional analytic expressions			
Ionic diffusivity	$D_{l,\text{eff}} = \frac{\epsilon_{l,\text{neg}}}{\tau_{\text{neg}}} D_l$	$D_{l,\text{eff}} = \frac{\epsilon_{l,\text{sep}}}{\tau_{\text{sep}}} D_l$	$D_{l,\text{eff}} = \frac{\epsilon_{l,\text{pos}}}{\tau_{\text{pos}}} D_l$
Ionic conductivity	$\kappa_{l,\text{eff}} = \frac{\epsilon_{l,\text{neg}}}{\tau_{\text{neg}}} \kappa_l$	$\kappa_{l,\text{eff}} = \frac{\epsilon_{l,\text{sep}}}{\tau_{\text{sep}}} \kappa_l$	$\kappa_{l,\text{eff}} = \frac{\epsilon_{l,\text{pos}}}{\tau_{\text{pos}}} \kappa_l$
Electronic conductivity	$\sigma_{s,\text{eff}} = \epsilon_{s,\text{neg}} \sigma_{s,\text{neg}}$	n/a	$\sigma_{s,\text{eff}} = \epsilon_{s,\text{pos}} \sigma_{s,\text{pos}}$
Reaction kinetics	$i_n = \frac{i_0\left[\exp\left(\frac{\alpha_a F}{RT}\eta\right)-\exp\left(\frac{\alpha_c F}{RT}\eta\right)\right]}{1+\frac{c_{s,\text{lim}}}{\Delta c_s}\exp\left(\frac{\alpha_a F}{RT}\eta\right)}$	n/a	$i_n = \frac{i_0\left[\exp\left(\frac{\alpha_a F}{RT}\eta\right)-\exp\left(\frac{\alpha_c F}{RT}\eta\right)\right]}{1+\left(\frac{c_{l,\text{lim}}}{\Delta c_l}+\frac{c_{s,\text{lim}}}{\Delta c_s}\right)\exp\left(\frac{\alpha_c F}{RT}\eta\right)}$
Exchange current density	$i_0 = F k_{\text{neg}}\left(\frac{c_l}{c_{l,\text{ref}}}\right)^{\alpha_a}$ $\cdot (c_{s,\text{max, neg}}-c_{s,\text{surf}})^{\alpha_a}(c_{s,\text{surf}})^{\alpha_c}$	n/a	$i_0 = F k_{\text{pos}}\left(\frac{c_l}{c_{l,\text{ref}}}\right)^{\alpha_a}$ $\cdot (c_{s,\text{max, pos}}-c_{s,\text{surf}})^{\alpha_a}(c_{s,\text{surf}})^{\alpha_c}$
Reaction overpotential	$\eta = \Phi_s - \Phi_l - \Delta\Phi_{s,\text{film}} - E_{\text{eq, neg}}$	n/a	$\eta = \Phi_s - \Phi_l - E_{\text{eq, pos}}$
*Boundary conditions**			
Species 2nd (liquid)	$\nabla c_l\vert_{x=0} = 0$	n/a	$\nabla c_l\vert_{x=l_{\text{neg}}+l_{\text{sep}}+l_{\text{pos}}} = 0$
Species 2nd (solid)	$\left.\frac{\partial c_s}{\partial r}\right\vert_{r=0} = 0 \quad \left.\frac{\partial c_s}{\partial r}\right\vert_{r=r_{\text{p, neg}}} = -\frac{i_n}{F D_{s,\text{neg}}}$	n/a	$\left.\frac{\partial c_s}{\partial r}\right\vert_{r=0} = 0 \quad \left.\frac{\partial c_s}{\partial r}\right\vert_{r=r_{\text{p, pos}}} = -\frac{i_n}{F D_{s,\text{pos}}}$
Potential 2nd (liquid)	$\nabla \Phi_l\vert_{x=0} = 0$	n/a	$\nabla \Phi_l\vert_{x=l_{\text{neg}}+l_{\text{sep}}+l_{\text{pos}}} = 0$
Potential** 1st (solid)	$\Phi_s\vert_{x=0} = 0$	n/a	$\Phi_s\vert_{x=l_{\text{neg}}+l_{\text{sep}}+l_{\text{pos}}} = 10^{-6}\,\text{V}$
	$\Phi_s\vert_{x=0} = \Phi_{\text{cc, neg}}$		$\Phi_s\vert_{x=l_{\text{neg}}+l_{\text{sep}}+l_{\text{pos}}} = \Phi_{\text{cc, pos}}$
Potential 2nd (solid)	$\nabla \Phi_s\vert_{x=l_{\text{neg}}} = 0$	n/a	$\nabla \Phi_s\vert_{x=l_{\text{neg}}+l_{\text{sep}}} = 0$
Derived quantities			
Heat source	$\dot{q}_{\text{p2D}} = \left[i_{\text{p2D}} E_{\text{p2D}} - \left(\int_{l_{0,\text{neg}}}^{l_{1,\text{neg}}}(a_{\text{neg}} i_n E_{\text{eq, neg, ave}})\,dx + \int_{l_{0,\text{pos}}}^{l_{1,\text{pos}}}(a_{\text{pos}} i_n E_{\text{eq, pos, ave}})\,dx\right)\right]$ $+ \left(\int_{l_{0,\text{neg}}}^{l_{1,\text{neg}}}\left(a_{\text{neg}} i_n T \frac{dE_{\text{eq, neg, ave}}}{dT}\right)dx + \int_{l_{0,\text{pos}}}^{l_{1,\text{pos}}}\left(a_{\text{pos}} i_n T \frac{dE_{\text{eq, pos, ave}}}{dT}\right)dx\right)$		

*indicated as first (Dirichlet) and second order (Neumann) boundary conditions.
**alternatively used for p2D model and coupled model.

Table A3. Main variables and governing partial differential equations solved within each domain of the 2D electrical model as well as prevailing boundary conditions including derived quantities.

Description	Negative current collector (cc, neg)	Positive current collector (cc, pos)
Variables and mathematical operators		
	$\Phi_{\text{cc, neg}}(x',y',t)$	$\Phi_{\text{cc, pos}}(x',y',t)$
	$\sigma_{\text{cc, neg}} := \begin{bmatrix} \sigma_{\text{cc, neg}} & 0 \\ 0 & \sigma_{\text{cc, neg}} \end{bmatrix}$	$\sigma_{\text{cc, pos}} := \begin{bmatrix} \sigma_{\text{cc, pos}} & 0 \\ 0 & \sigma_{\text{cc, pos}} \end{bmatrix}$
		$x' \in [0;\, w_{\text{ele}}]$
		$y' \in [0;\, h_{\text{ele}}]$
		$\nabla := \left(\frac{\partial}{\partial x'},\, \frac{\partial}{\partial y'}\right)^{\text{T}}$
Governing partial differential equations		
Charge balance	$\sigma_{\text{cc, neg}} \nabla^2 \Phi_{\text{cc, neg}} = -\frac{2\cdot i_{\text{p2D}}}{l_{\text{cc, neg}}}$	$\sigma_{\text{cc, pos}} \nabla^2 \Phi_{\text{cc, pos}} = \frac{2\cdot i_{\text{p2D}}}{l_{\text{cc, pos}}}$
	$\int\left(\sigma_{\text{cc, pos}} \cdot \frac{\partial \Phi_{\text{cc, pos}}}{\partial y'}\vert_{y'=h_{\text{ele}}} \cdot w_{\text{ele}} \cdot \frac{l_{\text{cc, pos}}}{2}\right)$	$dx' = \sum_i i_{\text{p2D},i} \cdot A_{\text{p2D},i}$
Boundary conditions		
Potential 1st	$\Phi_{\text{cc, neg}}\vert_{y'=0} = 0$	$\Phi_{\text{cc, pos}}\vert_{y'=h_{\text{ele}}} = 10^{-6}\,\text{V}$
Potential 2nd	$\frac{\partial \Phi_{\text{cc, neg}}}{\partial x'}\vert_{x'=0 \wedge x'=w_{\text{ele}}} = 0$	$\frac{\partial \Phi_{\text{cc, pos}}}{\partial x'}\vert_{x'=0 \wedge x'=w_{\text{ele}}} = 0$
Derived quantities		
Heat source	$\dot{q}_{\text{cc, neg}} = l_{\text{cc, neg}} \cdot \sigma_{\text{cc, neg}} \cdot (\nabla \Phi_{\text{cc, neg}})^2$	$\dot{q}_{\text{cc, pos}} = l_{\text{cc, pos}} \cdot \sigma_{\text{cc, pos}} \cdot (\nabla \Phi_{\text{cc, pos}})^2$

$$\frac{dE_{eq,\,pos}}{dT} = \frac{-2.445\times10^{-3}y^2 + 3.4961\times10^{-3}y - 1.4125\times10^{-3}}{y^2 - 2.7564y + 3.9766} \qquad [A2]$$

$$D_{s,\,neg} = 8\times10^{-14}\cdot\exp\left(\frac{2987\,\text{K}\cdot(T-298.15\,\text{K})}{(T\cdot298.15\,\text{K})}\right) \qquad [A3]$$

$$D_{s,\,pos} = 0.25\times10^{-14}\cdot\exp\left(\frac{2987\,\text{K}\cdot(T-298.15\,\text{K})}{(T\cdot298.15\,\text{K})}\right) \qquad [A4]$$

$$\kappa_l = 4.7557\times10^2\cdot\exp\left(\frac{-1.557\times10^3}{T}\right)\cdot\left(\frac{c_l}{1.173\times10^4\cdot\exp\left(\frac{-5.7251\times10^2}{T}\right)}\right)^{0.73}$$

$$\cdot\exp\left(-\left(\frac{c_l}{1.173\times10^4\cdot\exp\left(\frac{-5.7251\times10^2}{T}\right)}\right)^{1.73}\right) \qquad [A5]$$

$$D_l = 3.729\times10^{-9}\cdot\exp\left(-5.0646\times10^{-4}\cdot c_l + \frac{1.25\times10^2}{2.2879\times10^2 + 5.0051\times10^{-3}\cdot c_l - T}\right)$$
$$[A6]$$

$$(1-t_+)\cdot\text{TDF} = (1-t_+)\cdot\left(1+\frac{\partial \ln f_\pm}{\partial c_l}\right) =$$

$$2.4174\times10^{-3}\cdot\exp\left(\frac{-3.3972\times10^3}{1.0732\times10^3 - T}\right)\cdot c_l^{1.5} - 7.5895\times10^{-3}\cdot c_l^{0.5} + 6.01\times10^{-1}$$
$$[A7]$$

$$\sigma_{cc,\,neg} = \frac{5.96\times10^7}{1 + 3.383\times10^{-3}(T - 293.15\,\text{K})} \qquad [A8]$$

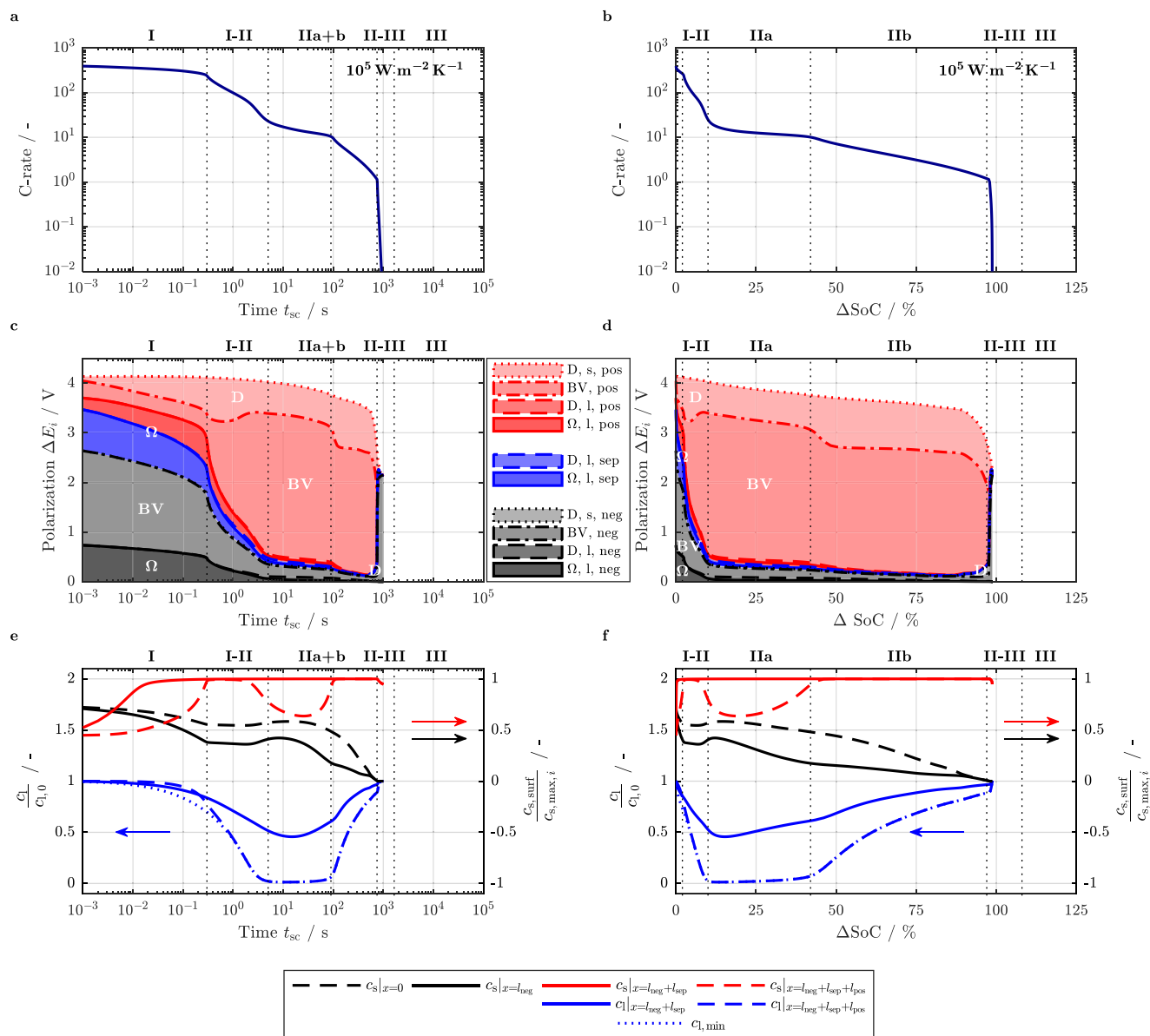$$\sigma_{cc,\,pos} = \frac{3.78\times10^7}{1 + 4.290\times10^{-3}(T - 293.15\,\text{K})} \qquad [A9]$$

Figure A1. Predicted phases of a short circuit during a hard short circuit event for a cooling condition of 10^5 W m^{-2} K^{-1} with respect to electrode area and a coolant temperature of 25°C observed in C-rate (top: a and b), the corresponding polarization throughout the electrodes and separator (middle: c and d) resulting from the normalized solid (surface) and liquid phase concentration (average) at distinct locations of the cell (bottom: e and f) as a function of short circuit duration (left: a, c, and e) and as a function of normalized discharged capacity (right: b, d, and f).

Table A4. Main variables and governing partial differential equations solved within the 3D thermal model as well as prevailing boundary conditions and derived quantities.

Description	Jelly roll (spiral part)	Jelly roll (linear part) Electrode stack
Variables and mathematical operators		

$$\boldsymbol{T}\left(r'', \psi'', z'', t\right)$$

$$\boldsymbol{\lambda} = \begin{bmatrix} \lambda_\perp & 0 & 0 \\ 0 & \lambda_\| & 0 \\ 0 & 0 & \lambda_\| \end{bmatrix}$$

$$\nabla := \left(\frac{\partial}{\partial r''}, \frac{\partial}{\partial \psi''}, \frac{\partial}{\partial z''}\right)^\mathrm{T}$$

$$\boldsymbol{T}\left(x'', y'', z'', t\right)$$

$$\boldsymbol{\lambda} = \begin{bmatrix} \lambda_\| & 0 & 0 \\ 0 & \lambda_\perp & 0 \\ 0 & 0 & \lambda_\| \end{bmatrix}$$

$$\nabla := \left(\frac{\partial}{\partial x''}, \frac{\partial}{\partial y''}, \frac{\partial}{\partial z''}\right)^\mathrm{T}$$

Governing partial differential equations

Heat balance

$$\rho_\mathrm{layer} c_{p,\,\mathrm{layer}} \frac{\partial \boldsymbol{T}}{\partial t} = \boldsymbol{\lambda} \nabla^2 \boldsymbol{T} + \frac{\dot{\boldsymbol{q}}}{l_\mathrm{layer}}$$

Boundary conditions
Temperature 2$^\mathrm{nd}$

$$-\boldsymbol{\lambda} \cdot \nabla \boldsymbol{T}|^\Gamma \cdot \mathbf{n} = 0 \vee -\boldsymbol{\lambda} \cdot \nabla \boldsymbol{T}|^\Gamma \cdot \mathbf{n} = h_\mathrm{c}\left(T_\infty - \boldsymbol{T}|^\Gamma\right)$$

Derived quantities

Heat source

$$\frac{\dot{\boldsymbol{q}}}{l_\mathrm{layer}} = \frac{\chi_\mathrm{p2D}}{l_\mathrm{neg} + l_\mathrm{sep} + l_\mathrm{pos}} \cdot \dot{\boldsymbol{q}}_\mathrm{p2D} + \frac{\chi_\mathrm{cc,\,neg}}{l_\mathrm{cc,\,neg}} \cdot \dot{\boldsymbol{q}}_\mathrm{cc,\,neg} + \frac{\chi_\mathrm{cc,\,pos}}{l_\mathrm{cc,\,pos}} \cdot \dot{\boldsymbol{q}}_\mathrm{cc,\,pos}$$

$^\Gamma$ referring to the boundaries of the jelly roll or electrode stack.

ORCID

Alexander Rheinfeld ⓘ https://orcid.org/0000-0003-0995-7266
Johannes Sturm ⓘ https://orcid.org/0000-0001-8876-9989
Alexander Frank ⓘ https://orcid.org/0000-0001-8069-2948
Stephan Kosch ⓘ https://orcid.org/0000-0002-7469-9577
Andreas Jossen ⓘ https://orcid.org/0000-0003-0964-1405

References

1. G.-H. Kim, K. Smith, K.-J. Lee, S. Santhanagopalan, and A. Pesaran, Multi-Domain Modeling of Lithium-Ion Batteries Encompassing Multi-Physics in Varied Length Scales, *Journal of The Electrochemical Society*, **158**, A955 (2011).
2. R. E. Gerver and J. P. Meyers, Three-Dimensional Modeling of Electrochemical Performance and Heat Generation of Lithium-Ion Batteries in Tabbed Planar Configurations, *Journal of The Electrochemical Society*, **158**, A835 (2011).
3. M. Guo and R. E. White, A distributed thermal model for a Li-ion electrode plate pair, *Journal of Power Sources*, **221**, 334 (2013).
4. S. V. Erhard, P. J. Osswald, J. Wilhelm, A. Rheinfeld, S. Kosch, and A. Jossen, Simulation and Measurement of Local Potentials of Modified Commercial Cylindrical Cells, *Journal of The Electrochemical Society*, **162**, A2707 (2015).
5. S. V. Erhard et al., Simulation and Measurement of the Current Density Distribution in Lithium-Ion Batteries by a Multi-Tab Cell Approach, *Journal of The Electrochemical Society*, **164**, A6324 (2017).
6. B. Rieger, S. V. Erhard, S. Kosch, M. Venator, A. Rheinfeld, and A. Jossen, Multi-Dimensional Modeling of the Influence of Cell Design on Temperature, Displacement and Stress Inhomogeneity in Large-Format Lithium-Ion Cells, *Journal of The Electrochemical Society*, **163**, A3099 (2016).
7. S. Kosch, Y. Zhao, J. Sturm, J. Schuster, G. Mulder, E. Ayerbe, and A. Jossen, A Computationally Efficient Multi-Scale Model for Lithium-Ion Cells, *Journal of The Electrochemical Society*, **165**, A2374 (2018).
8. J. Sturm, A. Rheinfeld, I. Zilberman, F. B. Spingler, S. Kosch, F. Frie, and A. Jossen, Modeling and simulation of inhomogeneities in a 18650 nickel-rich, silicon-graphite lithium-ion cell during fast charging, *Journal of Power Sources*, **412**, 204 (2019).
9. K.-C. Chiu, C.-H. Lin, S.-F. Yeh, Y.-H. Lin, and K.-C. Chen, An electrochemical modeling of lithium-ion battery nail penetration, *Journal of Power Sources*, **251**, 254 (2014).
10. W. Zhao, G. Luo, and C.-Y. Wang, Modeling Nail Penetration Process in Large-Format Li-Ion Cells, *Journal of The Electrochemical Society*, **162**, A207 (2015).
11. R. Zhao, J. Liu, and J. Gu, Simulation and experimental study on lithium ion battery short circuit, *Applied Energy*, **173**, 29 (2016).
12. J. Xu, Y. Wu, and S. Yin, Investigation of effects of design parameters on the internal short-circuit in cylindrical lithium-ion batteries, *RSC Advances*, **7**, 14360 (2017).
13. R. Zhao, J. Liu, and J. Gu, A comprehensive study on Li-ion battery nail penetrations and the possible solutions, *Energy*, **123**, 392 (2017).
14. A. Rheinfeld, A. Noel, J. Wilhelm, A. Kriston, A. Pfrang, and A. Jossen, Quasi-Isothermal External Short Circuit Tests Applied to Lithium-Ion Cells: Part I. Measurements, *Journal of The Electrochemical Society*, **165**, A3427 (2018).
15. A. Rheinfeld, J. Sturm, A. Noel, J. Wilhelm, A. Kriston, A. Pfrang, and A. Jossen, Quasi-Isothermal External Short Circuit Tests Applied to Lithium-Ion Cells: Part

16. J. Mao, W. Tiedemann, and J. Newman, Simulation of Li-ion Cells by Dualfoil Model under Constant-Resistance Load, *ECS Transactions*, **58**, 71 (2014).
17. J. Mao, W. Tiedemann, and J. Newman, Simulation of temperature rise in Li-ion cells at very high currents, *Journal of Power Sources*, **271**, 444 (2014).
18. J. Newman and W. Tiedemann, Potential and Current Distribution in Electrochemical Cells: Interpretation of the Half–Cell Voltage Measurements as a Function of Reference–Electrode Location, *Journal of The Electrochemical Society*, **140**, 1961 (1993).
19. U. S. Kim, C. B. Shin, and C.-S. Kim, Effect of electrode configuration on the thermal behavior of a lithium-polymer battery, *Journal of Power Sources*, **180**, 909 (2008).
20. S. Allu, S. Kalnaus, W. Elwasif, S. Simunovic, J. A. Turner, and S. Pannala, A new open computational framework for highly-resolved coupled three-dimensional multiphysics simulations of Li-ion cells, *Journal of Power Sources*, **246**, 876 (2014).
21. A. Rheinfeld, S. Kosch, S. V. Erhard, P. J. Osswald, B. Rieger, and A. Jossen, Electro-Thermal Modeling of Large Format Lithium-Ion Pouch Cells: A Cell Temperature Dependent Linear Polarization Expression, *Journal of The Electrochemical Society*, **163**, A3046 (2016).
22. S. Kosch, A. Rheinfeld, S. V. Erhard, and A. Jossen, An extended polarization model to study the influence of current collector geometry of large-format lithium-ion pouch cells, *Journal of Power Sources*, **342**, 666 (2017).
23. K. Smith, G.-H. Kim, E. Darcy, and A. Pesaran, Thermal/electrical modeling for abuse-tolerant design of lithium ion modules, *International Journal of Energy Research*, **34**, 204 (2010).
24. M. Guo and R. E. White, Mathematical model for a spirally-wound lithium-ion cell, *Journal of Power Sources*, **250**, 220 (2014).
25. S. Goutam, A. Nikolian, J. Jaguemont, J. Smekens, N. Omar, P. van Dan Bossche, and J. van Mierlo, Three-dimensional electro-thermal model of li-ion pouch cell: Analysis and comparison of cell design factors and model assumptions, *Applied Thermal Engineering*, **126**, 796 (2017).
26. B. S. Haran, B. N. Popov, and R. E. White, Determination of the hydrogen diffusion coefficient in metal hydrides by impedance spectroscopy, *Journal of Power Sources*, **75**, 56 (1998).
27. N. Baba, H. Yoshida, M. Nagaoka, C. Okuda, and S. Kawauchi, Numerical simulation of thermal behavior of lithium-ion secondary batteries using the enhanced single particle model, *Journal of Power Sources*, **252**, 214 (2014).
28. G. Fan, K. Pan, G. L. Storti, M. Canova, J. Marcicki, and X. G. Yang, A Reduced-Order Multi-Scale, Multi-Dimensional Model for Performance Prediction of Large-Format Li-Ion Cells, *Journal of The Electrochemical Society*, **164**, A252 (2017).
29. S. Khaleghi Rahimian, S. Rayman, and R. E. White, Extension of physics–based single particle model for higher charge-discharge rates, *Journal of Power Sources*, **224**, 180 (2013).
30. K. Somasundaram, E. Birgersson, and A. S. Mujumdar, Thermal–electrochemical model for passive thermal management of a spiral-wound lithium-ion battery, *Journal of Power Sources*, **203**, 84 (2012).
31. K.-J. Lee, K. Smith, A. Pesaran, and G.-H. Kim, Three dimensional thermal-, electrical-, and electrochemical-coupled model for cylindrical wound large format lithium-ion batteries, *Journal of Power Sources*, **241**, 20 (2013).
32. W. Zhao, G. Luo, and C.-Y. Wang, Effect of tab design on large-format Li-ion cell performance, *Journal of Power Sources*, **257**, 70 (2014).

33. J. Li, Y. Cheng, L. Ai, M. Jia, S. Du, B. Yin, S. Woo, and H. Zhang, 3D simulation on the internal distributed properties of lithium-ion battery with planar tabbed configuration, *Journal of Power Sources*, **293**, 993 (2015).

34. M. Doyle, T. F. Fuller, and J. Newman, Modeling of Galvanostatic Charge and Discharge of the Lithium/Polymer/Insertion Cell, *Journal of The Electrochemical Society*, **140**, 1526 (1993).

35. J. Newman and K. E. Thomas-Alyea, *Electrochemical Systems*, 3rd ed., Wiley-Interscience: Hoboken, NJ, USA, 2004.

36. G. Zhang, L. Cao, S. Ge, C.-Y. Wang, C. E. Shaffer, and C. D. Rahn, In Situ Measurement of Radial Temperature Distributions in Cylindrical Li-Ion Cells, *Journal of The Electrochemical Society*, **161**, A1499 (2014).

37. T. Amietszajew, E. McTurk, J. Fleming, and R. Bhagat, Understanding the limits of rapid charging using instrumented commercial 18650 high-energy Li-ion cells, *Electrochimica Acta*, **263**, 346 (2018).

38. W. Q. Li, Z. G. Qu, Y. L. He, and Y. B. Tao, Experimental study of a passive thermal management system for high-powered lithium ion batteries using a porous metal foam saturated with phase change materials, *Journal of Power Sources*, **255**, 9 (2014).

39. Y. Lai, S. Du, L. Ai, L. Ai, Y. Cheng, Y. Tang, and M. Jia, Insight into heat generation of lithium ion batteries based on the electrochemical-thermal model at high discharge rates, *International Journal of Hydrogen Energy*, **40**, 13039 (2015).

40. W. Mei, H. Chen, J. Sun, and Q. Wang, The effect of electrode design parameters on battery performance and optimization of electrode thickness based on the electrochemical–thermal coupling model, *Sustainable Energy & Fuels*, **3**, 148 (2019).

41. D. A. H. McCleary, J. P. Meyers, and B. Kim, Three-Dimensional Modeling of Electrochemical Performance and Heat Generation of Spirally and Prismatically Wound Lithium-Ion Batteries, *Journal of The Electrochemical Society*, **160**, A1931 (2013).

42. DIN Deutsches Institut für Normung e.V., Electrically propelled road vehicles - Battery systems - Design specifications for Lithium-Ion battery cells. 2016-11.

43. T. D. Hatchard, D. D. MacNeil, A. Basu, and J. R. Dahn, Thermal Model of Cylindrical and Prismatic Lithium-Ion Cells, *Journal of The Electrochemical Society*, **148**, A755 (2001).

44. R. Spotnitz and J. Franklin, Abuse behavior of high-power, lithium-ion cells, *Journal of Power Sources*, **113**, 81 (2003).

45. G.-H. Kim, A. Pesaran, and R. Spotnitz, A three-dimensional thermal abuse model for lithium-ion cells, *Journal of Power Sources*, **170**, 476 (2007).

46. S. Hildebrand, A. Rheinfeld, A. Friesen, J. Haetge, F. M. Schappacher, A. Jossen, and M. Winter, Thermal Analysis of LiNi$_{0.4}$Co$_{0.2}$Mn$_{0.4}$O$_2$/Mesocarbon Microbeads Cells and Electrodes: State-of-Charge and State-of-Health Influences on Reaction Kinetics, *Journal of The Electrochemical Society*, **165**, A104 (2018).

47. L. O. Valøen and J. N. Reimers, Transport Properties of LiPF$_6$-Based Li-Ion Battery Electrolytes, *Journal of The Electrochemical Society*, **152**, A882 (2005).

48. M. N. Richard and J. R. Dahn, Accelerating Rate Calorimetry Study on the Thermal Stability of Lithium Intercalated Graphite in Electrolyte. I. Experimental, *Journal of The Electrochemical Society*, **146**, 2068 (1999).

49. M. N. Richard and J. R. Dahn, Accelerating Rate Calorimetry Study on the Thermal Stability of Lithium Intercalated Graphite in Electrolyte. II. Modeling the Results and Predicting Differential Scanning Calorimeter Curves, *Journal of The Electrochemical Society*, **146**, 2078 (1999).

50. L. Ma, M. Nie, J. Xia, and J. R. Dahn, A systematic study on the reactivity of different grades of charged Li[Ni$_x$Mn$_y$Co$_z$]O$_2$ with electrolyte at elevated temperatures using accelerating rate calorimetry, *Journal of Power Sources*, **327**, 145 (2016).

51. C. Kupper, S. Spitznagel, H. Döring, M. A. Danzer, C. Gutierrez, A. Kvasha, and W. G. Bessler, Combined modeling and experimental study of the high-temperature behavior of a lithium-ion cell: Differential scanning calorimetry, accelerating rate calorimetry and external short circuit, *Electrochimica Acta*, **306**, 209 (2019).

52. A. Kriston, A. Pfrang, H. Döring, B. Fritsch, V. Ruiz, I. Adanouj, T. Kosmidou, J. Ungeheuer, and L. Boon-Brett, External short circuit performance of Graphite-LiNi$_{1/3}$Co$_{1/3}$Mn$_{1/3}$O$_2$ and Graphite-LiNi$_{0.8}$Co$_{0.15}$Al$_{0.05}$O$_2$ cells at different external resistances, *Journal of Power Sources*, **361**, 170 (2017).

53. B. Barnett, D. Ofer, S. Sriramulu, and R. Stringfellow, In *Encyclopedia of Sustainability Science and Technology*, R. A. Meyers, Ed., Springer: New York, NY, USA, ; pp 6097, 2012.

54. T. M. Bandhauer, S. Garimella, and T. F. Fuller, Electrochemical-Thermal Modeling to Evaluate Battery Thermal Management Strategies: I. Side Cooling, *Journal of The Electrochemical Society*, **162**, A125 (2015).

55. I. A. Hunt, Y. Zhao, Y. Patel, and G. J. Offer, Surface Cooling Causes Accelerated Degradation Compared to Tab Cooling for Lithium-Ion Pouch Cells, *Journal of The Electrochemical Society*, **163**, A1846 (2016).

56. T. M. Bandhauer, S. Garimella, and T. F. Fuller, Electrochemical-Thermal Modeling to Evaluate Battery Thermal Management Strategies: II. Edge and Internal Cooling, *Journal of The Electrochemical Society*, **162**, A137 (2015).

57. C.-F. Chen, A. Verma, and P. P. Mukherjee, Probing the Role of Electrode Microstructure in the Lithium-Ion Battery Thermal Behavior, *Journal of The Electrochemical Society*, **164**, E3146 (2017).

58. D. J. Noelle, M. Wang, A. V. Le, Y. Shi, and Y. Qiao, Internal resistance and polarization dynamics of lithium-ion batteries upon internal shorting, *Applied Energy*, **212**, 796 (2018).

59. M. Fleischhammer, T. Waldmann, G. Bisle, B.-I. Hogg, and M. Wohlfahrt-Mehrens, Interaction of cyclic aging at high-rate and low temperatures and safety in lithium-ion batteries, *Journal of Power Sources*, **274**, 432 (2015).

60. J. N. Reimers, Accurate and Efficient Treatment of Foil Currents in a Spiral Wound Li-Ion Cell, *Journal of The Electrochemical Society*, **161**, A118 (2014).

61. H. Lundgren, P. Svens, H. Ekström, C. Tengstedt, J. Lindström, M. Behm, and G. Lindbergh, Thermal Management of Large-Format Prismatic Lithium-Ion Battery in PHEV Application, *Journal of The Electrochemical Society*, **163**, A309 (2016).

62. M. Xu, Z. Zhang, X. Wang, L. Jia, and L. Yang, A pseudo three-dimensional electrochemical–thermal model of a prismatic LiFePO$_4$ battery during discharge process, *Energy*, **80**, 303 (2015).

63. F. Bahiraei, A. Fartaj, and G.-A. Nazri, Electrochemical-thermal Modeling to Evaluate Active Thermal Management of a Lithium-ion Battery Module, *Electrochimica Acta*, **254**, 59 (2017).

64. Y. Reynier, R. Yazami, and B. Fultz, The entropy and enthalpy of lithium intercalation into graphite, *Journal of Power Sources*, **119–121**, 850 (2003).

65. W. Lu, I. Belharouak, D. Vissers, and K. Amine, In Situ Thermal Study of Li$_{1+x}$[Ni$_{1/3}$Co$_{1/3}$ Mn$_{1/3}$]$_{1-x}$O$_2$ Using Isothermal Micro-clorimetric Techniques, *Journal of The Electrochemical Society*, **153**, A2147 (2006).

66. F. A. Wolff and J. H. Dellinger, The electrical conductivity of commercial copper, *Proceedings of the American Institute of Electrical Engineers*, **29**, 1981 (1910).

67. D. G. Giancoli, *Physics: Principles with application*, 4th edition, Prentice Hall: Englewood Cliffs, NJ, USA, 1995.

68. J. Christensen, V. Srinivasan, and J. Newman, Optimization of Lithium Titanate Electrodes for High-Power Cells, *Journal of The Electrochemical Society*, **153**, A560 (2006).

69. S. C. Chen, C. C. Wan, and Y. Y. Wang, Thermal analysis of lithium-ion batteries, *Journal of Power Sources*, **140**, 111 (2005).